THE UNIVERSITY OF ALABAMA® | University Libraries

Evaluating Systematic Dependencies of Type Ia Supernovae: The Influence of Central Density

Brendan K. Krueger – The State University of New York

Aaron P. Jackson – The State University of New York

Alan C. Calder – The State University of New York

Dean M. Townsley – The University of Alabama

Edward F. Brown – Michigan State University

Francis X. Timmes – Arizona State University

Deposited 08/23/2018

Citation of published version:

Krueger, B., et al. (2012): Evaluating Systematic Dependencies of Type Ia Supernovae: The Influence of Central Density. *The Astrophysical Journal*, 757(2).
http://dx.doi.org/10.1088/0004-637X/757/2/175

© 2012. The American Astronomical Society. All rights reserved. Printed in the U.S.A

The Astrophysical Journal, 757:175 (23pp), 2012 October 1 doi:10.1088/0004-637X/757/2/175
© 2012. The American Astronomical Society. All rights reserved. Printed in the U.S.A.

EVALUATING SYSTEMATIC DEPENDENCIES OF TYPE Ia SUPERNOVAE: THE INFLUENCE OF CENTRAL DENSITY

Brendan K. Krueger[1], Aaron P. Jackson[1,7], Alan C. Calder[1,2], Dean M. Townsley[3], Edward F. Brown[4,5], and Francis X. Timmes[5,6]
[1] Department of Physics & Astronomy, The State University of New York–Stony Brook, Stony Brook, NY, USA; brendan.krueger@stonybrook.edu
[2] New York Center for Computational Sciences, The State University of New York–Stony Brook, Stony Brook, NY, USA
[3] Department of Physics and Astronomy, The University of Alabama, Tuscaloosa, AL, USA
[4] Department of Physics and Astronomy, Michigan State University, East Lansing, MI, USA
[5] The Joint Institute for Nuclear Astrophysics, Notre Dame, IN, USA
[6] School of Earth and Space Exploration, Arizona State University, Tempe, AZ, USA
Received 2012 February 13; accepted 2012 August 3; published 2012 September 17

ABSTRACT

We present a study exploring a systematic effect on the brightness of Type Ia supernovae using numerical models that assume the single-degenerate paradigm. Our investigation varied the central density of the progenitor white dwarf at flame ignition, and considered its impact on the explosion yield, particularly the production and distribution of radioactive ^{56}Ni, which powers the light curve. We performed a suite of two-dimensional simulations with randomized initial conditions, allowing us to characterize the statistical trends that we present. The simulations indicate that the production of Fe-group material is statistically independent of progenitor central density, but the mass of stable Fe-group isotopes is tightly correlated with central density, with a decrease in the production of ^{56}Ni at higher central densities. These results imply that progenitors with higher central densities produce dimmer events. We provide details of the post-explosion distribution of ^{56}Ni in the models, including the lack of a consistent centrally located deficit of ^{56}Ni, which may be compared to observed remnants. By performing a self-consistent extrapolation of our model yields and considering the main-sequence lifetime of the progenitor star and the elapsed time between the formation of the white dwarf and the onset of accretion, we develop a brightness–age relation that improves our prediction of the expected trend for single degenerates and we compare this relation with observations.

Key words: hydrodynamics – nuclear reactions, nucleosynthesis, abundances – supernovae: general – white dwarfs

Online-only material: color figures

1. INTRODUCTION

Type Ia supernovae (SNe Ia) are bright, transient astronomical events identified by a peak-light spectrum showing no evidence of hydrogen but absorption lines of singly ionized silicon (Minkowski 1941; Filippenko 1997). These events follow from explosive thermonuclear burning of degenerate stellar material composed principally of C and O, which synthesizes $\sim$0.6 $M_{\odot}$ of radioactive ^{56}Ni. The decay of this ^{56}Ni powers the light curve (Truran et al. 1967; Colgate & McKee 1969; Arnett 1982; Pinto & Eastman 2000).

The progenitor systems of these explosions remain the subject of considerable debate and active research. Observations, however, indicate that these events largely form a homogeneous class. Phillips (1993) identified a relationship between the maximum *B*-band magnitude of an event and its rate of decline. This "brighter equals broader" relationship has been extended to additional bands with templates from nearby events, allowing these events to be calibrated as an extension of the astronomical distance ladder (see Jha et al. 2007 for a description). This property, along with the brightness of SNe Ia, which makes them visible over great distances, enables the use of SNe Ia to probe the structure and expansion history of the universe, allowing studies of various cosmological models' parameters (Riess et al. 1998; Perlmutter et al. 1999; Albrecht et al. 2006; Kirshner 2010), with recent work constraining cosmological parameters to within a few percent (Riess et al. 2011; Sullivan et al. 2011). Recent observational studies of SNe Ia have begun to correct for correlations of the brightness of an SN Ia with properties of the host galaxy (Conley et al. 2011). Many SN Ia observations are restricted to broadband photometry, so knowledge of host galaxy properties is correlated. The inability to deconvolve these properties from each other is among the larger sources of uncertainty in cosmological constraints from SNe Ia, so advancing the understanding of how brightness correlates with host galaxy properties may contribute significantly to reducing the uncertainties of cosmological parameters.

The brightness, and therefore "broadness," of an SN Ia is determined principally by the amount of ^{56}Ni synthesized during the explosion. Observations report that SNe Ia appear to have an intrinsic scatter of a few tenths of a magnitude after calibration, forcing a minimum uncertainty in any distances measured by using SNe Ia as standardizable candles (Jacoby et al. 1992; Kirshner 2010). An important goal of theoretical research into SNe Ia, from the standpoint of cosmology, is to understand the sources of scatter and to identify potential systematic biases by studying the effects of various properties on the mechanism and nucleosynthetic yield of the SN Ia. The surrounding stellar population, the metallicity and mass of the progenitor, the thermodynamic state of the progenitor, the cooling and accretion history of the progenitor, and other parameters are known to affect the light curves of SNe Ia; the role of these "secondary" parameters is the subject of considerable study (e.g., Röpke et al. 2006; Höflich et al. 2010). Additionally, many of these effects may be interconnected in complex ways (Domínguez et al. 2001; Lesaffre et al. 2006; Townsley et al. 2009).

Observational campaigns are gathering information about SNe Ia at an unprecedented rate. Scannapieco & Bildsten (2005) and Mannucci et al. (2006) showed that the delay time

[7] Current address: Laboratory for Computational Physics and Fluid Dynamics, Naval Research Laboratory, Washington, DC, USA.

(elapsed time between star formation and the supernova event) data are best fit by a bimodal delay time distribution (DTD) with a prompt component that tracks less than 1 Gyr after star formation and a tardy component that occurs several Gyr later. Gallagher et al. (2008) demonstrate a correlation between brighter SNe Ia and shorter delay times, which they state is consistent with the bimodality described by Mannucci et al., but also with a continuous relation. Howell et al. (2009), Neill et al. (2009), and Brandt et al. (2010) also find such a correlation between the delay time and brightness of an SN Ia. While the degeneracy of age and metallicity in observations could obscure these correlations, Howell et al. (2009) note that the scatter in brightness of this observed relation is unlikely to be explained by the effect of metallicity.

For this theoretical study, we adopt the model known as the single-degenerate paradigm. This model assumes that an SN Ia is the result of a thermonuclear disruption of a white dwarf (WD) in a mass-transferring binary system with either a main-sequence or red-giant companion star (see Branch et al. 1995; Filippenko 1997; Hillebrandt & Niemeyer 2000; Livio 2000; Röpke 2006; Li et al. 2011; Nugent et al. 2011; Bloom et al. 2012, and references therein). Recent observational evidence, however, suggests that other progenitors such as the merging of two WDs may explain many events (Scalzo et al. 2010; Yuan et al. 2010). In the single-degenerate scenario, the WD is formed when the primary star goes through a giant phase and expels a planetary nebula. Once the primary becomes a WD, it is initially not in contact with the companion star, and it slowly cools as thermal energy is radiated away. Once the companion star evolves and fills its Roche lobe, mass transfer begins to carry low-mass elements from the envelope of the companion to the surface of the WD. If the accretion rate exceeds $\sim 10^{-7}\ M_{\odot}\ \mathrm{yr}^{-1}$, the H-rich material can steadily burn (Nomoto et al. 2007) and the WD gains mass, which heats and compresses the WD, driving up both the temperature and density in the core. Once the temperature rises enough for carbon burning to begin, the core of the WD begins to convect; this is known as the "simmering" phase. This simmering phase lasts on the order of 10^3 yr, and ends when a flame is ignited, which occurs approximately when the eddy turnover time becomes shorter than the local nuclear runaway time. Our initial models attempt to parameterize the WD at the end of the simmering phase, just at the beginning of the thermonuclear deflagration, which will in turn cause an explosion that will disrupt the entire WD in an SN Ia.

The explosion mechanism we use (within the single-degenerate paradigm) is that of a deflagration-to-detonation transition (DDT). After ignition, the flame propagates as a subsonic deflagration for a while and then transitions to a supersonic detonation that rapidly consumes the star (Blinnikov & Khokhlov 1986; Woosley 1990; Khokhlov 1991; Höflich et al. 1995; Höflich & Khokhlov 1996; Khokhlov et al. 1997; Niemeyer & Woosley 1997; Höflich et al. 1998; Niemeyer 1999). We describe the details of our implementation of this explosion mechanism below.

In the single-degenerate paradigm, a longer delay time can be explained by a longer elapsed time between the formation of the WD and the onset of accretion. During this period, the WD is in isolation and cools, hence the moniker the "WD cooling time" (τ_{cool}). Following the cooling time is a period of accretion, during which the WD is compressed and heats, approaching the conditions for ignition of the thermonuclear runaway. The decrease in temperature during the cooling time, which is determined by τ_{cool}, influences the density structure of the WD just prior to ignition, with a longer τ_{cool} resulting in a higher central density when the core reaches the ignition temperature (Lesaffre et al. 2006). Thus, a correlation between central density and the brightness of an event would suggest a correlation between delay time and the brightness of an event.

In this manuscript, we expand on our earlier investigation on the effect of τ_{cool} on the brightness of the explosion. In Krueger et al. (2010) we reported that as the central density of the progenitor WD increases, the production of radioactive ^{56}Ni decreases due to increased neutronization rates, producing a dimmer event. Using the results of Lesaffre et al. (2006), we related the WD central density to τ_{cool} and were able to compare our results to the observations of Neill et al. (2009). Here we present additional details of our models, a statistical analysis of the results including the assessment of intrinsic scatter, the distribution of Fe-group elements (IGEs) within the remnant, and a potentially observable effect to demonstrate the connection between age, progenitor central density, and brightness. We also revised our previously reported trend in brightness with age to account for the main-sequence evolution of the WD progenitor.

In Section 2 we discuss the methodology of our suite of simulations, followed by details of the code we used to perform our simulations in Section 3. We present the results of our simulations in Section 4, and discuss how these results compare with previous studies in Section 5. Section 6 contains a brief summary and final conclusions.

2. METHODOLOGY

As described above, our explosion models assume that the DDT mechanism in which a flame ignited in the core propagates as a subsonic deflagration and then transitions to a detonation. We simulate an explosion from ignition through the detonation phase until burning effectively ceases. Our models are by necessity incomplete, however, in that we do not produce light curves and spectra with which we could compare to actual observations. Instead, we rely on the mass of ^{56}Ni synthesized in our models and compare this result from our simulations to ^{56}Ni masses inferred from observations (Howell et al. 2009).

For the study, we adopted the theoretical framework first applied in Townsley et al. (2009) for a statistical study of a suite of simulations performed with randomized initial conditions. We constructed a set of five progenitor models with different central densities ($\rho_{c,0}$), and therefore slightly different masses, and from these performed suites of two-dimensional (2D) simulations. For each progenitor model, we applied 30 sets of initial conditions consisting of randomized perturbations on an initially burned region. We refer to each of these 30 as a realization, each of which is seeded by a random number used to generate a unique power spectrum of spherical harmonics (see Appendix A for details of the realizations). The spectra are used as initial perturbations to a spherical "match head" in the center of the progenitor star. Each progenitor WD had the same seed values applied, resulting in the same 30 perturbations. This procedure allows us to characterize the intrinsic scatter in the models and check for systematic biases in the realizations across different progenitors, such as how the morphology of the initial conditions may influence the final result.

Complete details of our models and simulations follow, but we preface the description by mentioning that one limitation of our study is the use of 2D models and the parameterization

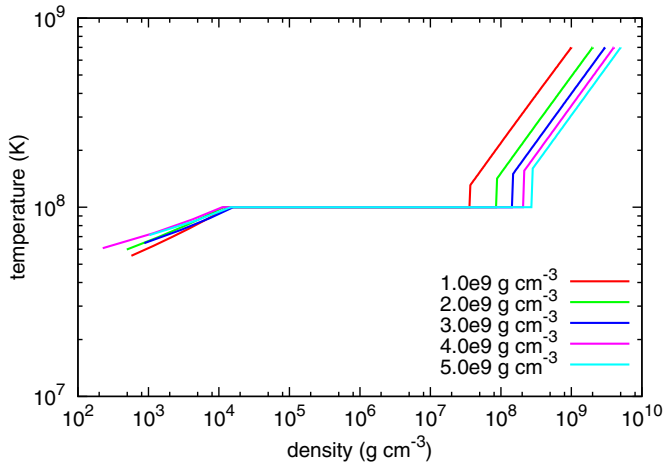

Figure 1. Structure of our progenitor WDs in ρ–T space. Below $\sim 10^4$ g cm^{-3} is the power-law atmosphere. In the center of the figure is the isothermal envelope, with the same temperature for all progenitors. In the upper right region of the figure is the adiabatic core; all five progenitors are isentropic in this region, but the value of the entropy varies between progenitors.

(A color version of this figure is available in the online journal.)

of inherently three-dimensional (3D) phenomena. In particular, 2D models lack any meaningful consideration of turbulence and its effect on the flame because the turbulence found in the interior of a simmering WD and its interaction with the flame are inherently 3D. The problem is compounded by the fact that this interaction occurs partially on unresolvable scales, necessitating the use of sub-grid-scale models (see Schmidt et al. 2006a, for an example).

There are two critical ways that omitting consideration of turbulence influences this work. The first is in the calculation of flame speeds during the deflagration phase. The burning model (described below) relies on an input flame speed to propagate a model flame during the deflagration. Turbulence will interact with this flame, stretching it and thereby boosting the burning rate (see Schmidt et al. 2006a, 2006b, and references therein). Our present models boost the input flame speed from tabulated laminar values to compensate for buoyancy effects (Townsley et al. 2009) but do not include the effect of turbulence–flame interactions (TFIs) for reasons discussed above. Effectively, we assume that the increase in flame surface (and hence the burning rate) is dominated by stretching due to buoyancy rather than turbulence.

The second critical way that omitting consideration of turbulence influences this work is in the criteria for the DDT (see Seitenzahl et al. 2011, and references therein). For this study, we parameterized the DDT criterion as a threshold density, $\rho_{\rm DDT}$, with a detonation initiated when the top of a rising plume of burned material reaches this density. As we describe below, this threshold density determines the duration of the deflagration and thus strongly influences the outcome of an explosion. Our a priori choice for this parameter led to higher than expected yields of radioactive ^{56}Ni, necessitating a rescaling of our results for comparison to observations. Confirmation of the trends we present from extrapolated results awaits a future study with a more consistent treatment of these issues.

2.1. Initial White Dwarf Models

As demonstrated by Lesaffre et al. (2006), for a given zero-age main-sequence mass, the properties of a progenitor WD such as central temperature and density at ignition of the deflagration

Table 1
Central Densities, Masses, and Radii of Progenitor WDs

$\rho_{c,0}$ (g cm^{-3})	$M_{\rm tot}$ ($M_\odot$)	$M_{\rm core}$ ($M_\odot$)	R (km)
1×10^9	1.345	1.180	2500
2×10^9	1.368	1.162	2076
3×10^9	1.379	1.144	1852
4×10^9	1.385	1.131	1716
5×10^9	1.389	1.121	1604

Table 2
Composition of the Progenitor WDs

Isotope	Mass Fraction	
	Core (%)	Envelope (%)
^{12}C	40	50
^{16}O	57	48
^{22}Ne	3	2

can be constructed as functions of $\tau_{\rm cool}$. We take the leading-order effect from varying $\tau_{\rm cool}$; that is, vary $\rho_{c,0}$ while holding all other parameters constant. This choice allows us to disentangle the effects of $\rho_{c,0}$ from the effects of other parameters. For our $\rho_{c,0}$, we chose 1–5 $\times 10^9$ g cm^{-3} in steps of 1×10^9 g cm^{-3}. We then constructed a series of five parameterized WD progenitor models in hydrostatic equilibrium.

Figure 1 presents the profiles of the progenitor WDs in the ρ–T plane. The core of each WD is isentropic due to convection, the intermediate ("envelope") region is isothermal due to the high conductivity of degenerate matter, and the outer ("atmosphere") region has a power-law temperature dependence that was chosen to mimic a radiative atmosphere. For a model to explode, the central temperature must be in the range where the carbon burning begins a runaway, which is approximately 7–8 $\times 10^8$ K. Varying the isothermal envelope temperature would have a relatively insignificant effect on the mass, as the envelope contains only a small fraction of the mass; primarily, the mass is set by $\rho_{c,0}$. Thus, we have chosen a central temperature at the low end of the carbon ignition range and allow the total mass to vary as a function of $\rho_{c,0}$. Table 1 shows the total mass ($M_{\rm tot}$) and mass of the isentropic core ($M_{\rm core}$) for each progenitor.

The core of each WD has a lower C/O ratio than the envelope; this is primarily due to the composition of different regions of the star at the end of the asymptotic giant branch (AGB) phase and the subsequent mixing of these regions, with additional contributions from the consumption of C during the simmering phase (Straniero et al. 2003; Piro & Bildsten 2008; Chamulak et al. 2008; Piro & Chang 2008). Our parameterized models for this study assume a fixed carbon abundance. As we plan to also study the dependence on central carbon abundance, we have maintained a clear separation between the central-density and the carbon-abundance studies by varying only central density and not the core carbon fraction. The composition discontinuity between the core and the envelope causes a temperature discontinuity (Piro & Chang 2008), shown by the short vertical line segments between the core and the envelope in Figure 1. The composition is listed in Table 2. We use ^{22}Ne as a placeholder to represent the neutron-rich isotopes present in an SN Ia. The abundance of ^{22}Ne is calibrated to achieve the electron-to-baryon ratio of the material present in an SN Ia, but sedimentation effects are not included. See Jackson et al. (2010), specifically Section 2, for a more detailed discussion.

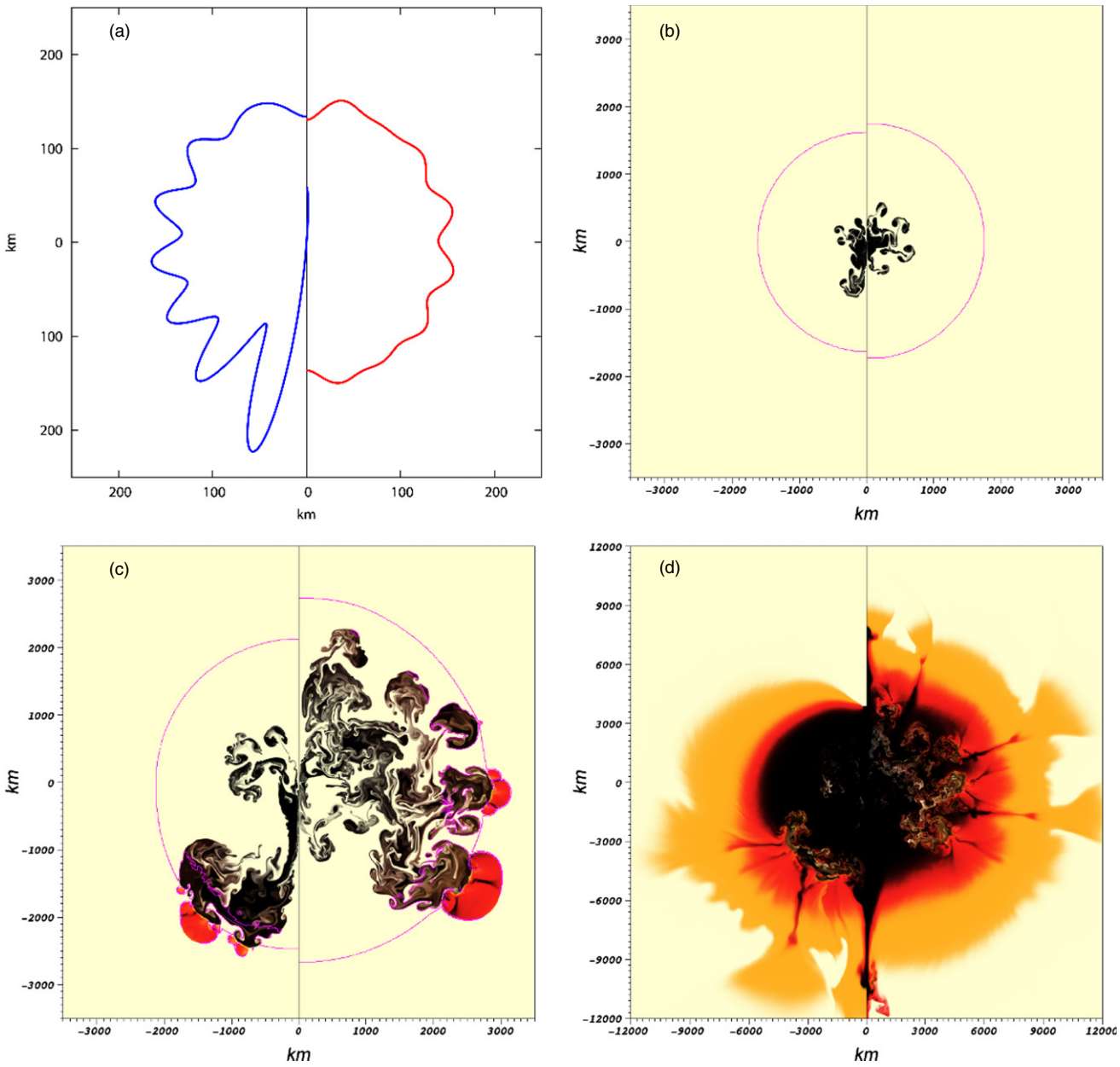

Figure 2. Illustrations of the phases of the DDT model of an SN Ia; each panel displays two of our realizations: 21 (left) and 10 (right). Panel (a) shows the initial flame surfaces; realization 21 has the greatest deviation from the mean radius, and realization 10 has the least deviation from the mean radius. Panels (b)–(d) are snapshots from our simulations, with $\rho_{c,0} = 3 \times 10^9$ g cm^{-3}; panel (b) shows the early deflagration phase, panel (c) shows the first DDT events, and panel (d) shows the later detonation phase. The colors represent the four stages of the burning model discussed in Section 3.1: cream represents unburned fuel, gold represents ash from carbon burning, red represents material in NSQE, and black represents material in NSE. Only in the detonation stage do the three burning processes separate out spatially; they are co-located during the deflagration. Our simulations extend to $\sim 6.5 \times 10^8$ km, but these images show only the inner regions; the spatial scale varies between panels, with only panels (b) and (c) having the same spatial extent in order to illustrate the expansion that occurs during the deflagration phase.

(A color version of this figure is available in the online journal.)

2.2. Ensemble of Simulations

The 30 unique realizations for each of our five progenitor models, consisting of a set of perturbations on the initially burned region, allowed us to perform a suite of 150 2D, axisymmetric simulations of SNe Ia. A simulation begins with a region of burned material at the center of the star with the perturbation from sphericity given as spherical harmonics with a prescribed range of $12 \leqslant \ell \leqslant 16$ and random amplitudes; the amplitudes for each realization are shown in Appendix A. Each realization has a unique seed (for the random number generator), allowing each realization to be applied to the five progenitor models. Figure 2(a) shows two example perturbations that span the space of the random perturbations. Realization 21, on the left, is representative of the "spikiest" initial conditions, i.e., the greatest deviation from the mean radius. Realization 10, on the right, is representative of the "smoothest" initial conditions, i.e., the smallest deviation from the mean radius.

3. THE SIMULATION CODE

The simulations were performed using a customized version of the FLASH code,[8] an Eulerian adaptive-mesh compressible hydrodynamics code developed by the ASC/Alliances Center

[8] Available from http://flash.uchicago.edu.

for Astrophysical Thermonuclear Flashes at the University of Chicago (Fryxell et al. 2000; Calder et al. 2002). The equation of state (EoS) that we use is the fully ionized electron–ion plasma EoS (Timmes & Swesty 2000; Fryxell et al. 2000). The version of FLASH used here is the same as that used in Jackson et al. (2010). Customizations perform two main functions: first, allowing the implementation of the energy release due to explosive carbon–oxygen fusion, in both deflagration and detonation propagation modes, as well as a provision for a transition from deflagration to detonation; and second, providing criteria for mesh refinement that capture the important physics with a suitable degree of efficiency. Details of various components are given by Townsley et al. (2007), Townsley et al. (2009), and Jackson et al. (2010), with important additional and supporting information on implementation of some pieces of physics in Calder et al. (2007) and Seitenzahl et al. (2009b).

As mentioned in the introductory material, the simulations implement a multi-dimensional version of the DDT model, in which the flame is born as a subsonic deflagration and later transitions to a supersonic detonation (Blinnikov & Khokhlov 1986; Woosley 1990; Khokhlov 1991; Höflich et al. 1995; Höflich & Khokhlov 1996; Khokhlov et al. 1997; Niemeyer & Woosley 1997; Höflich et al. 1998; Niemeyer 1999). The initial conditions prescribe the deflagration at the start of a simulation. As the deflagration proceeds, the flame is subject to fluid instabilities (Figure 2(b)), and when the top of a rising bubble reaches the threshold density, it is assumed to transition into a supersonic detonation (Figures 2(c) and (d); see Section 3.1.2 for details of the transition). See Townsley et al. (2009), Maeda et al. (2010), Jackson et al. (2010), Röpke et al. (2011), Seitenzahl et al. (2011), and references therein for examples of recent work assuming this explosion mechanism.

3.1. Burning Model

Since the carbon–oxygen fusion occurring in SNe Ia proceeds to nuclear statistical equilibrium (NSE), in which all reactions among all nuclides are, to good approximation, fast relative to the hydrodynamic timescales, the nuclear processing necessarily involves a large number of reactions and nuclides. This is especially true when calculating e^- capture on IGEs, as the overall effective e^- capture rate is a combination of contributions from captures on a wide variety of nuclides with comparable individual rates. As explored in our earlier work (Calder et al. 2007; Townsley et al. 2007; see also Khokhlov 2000), it is possible to abstract the burning process from hundreds of nuclides to just a few fluid state variables with appropriately chosen reaction dynamics and energetics computed using a large set of nuclides. This enables tremendous gains in computational efficiency, making 3D simulations and extensive 2D studies such as this feasible.

Our burning model consists of three reaction progress variables that describe conversion between four states. The first state is the initial, unburned mixture of ^{12}C, ^{16}O, and ^{22}Ne (representing general neutron excess, as described in Section 2.1), which we call fuel. The second state is the result of the ^{12}C fusing to roughly Si-group elements, which we call ash. The third state is the result of the remaining ^{16}O burning to Si-group elements, which we call nuclear statistical quasi-equilibrium (NSQE) material. The fourth and final state is the result of NSQE material relaxing to NSE, containing mostly IGEs. The three reaction progress variables are the following: $\phi_{\rm fa}$—carbon consumption, fuel to ash; $\phi_{\rm aq}$—oxygen consumption, ash to NSQE; and $\phi_{\rm qn}$—conversion of Si-group to Fe-group, NSQE to NSE.

Each variable evolves from 0 (unburned) to 1 (fully burned). We also require that $\phi_{\rm fa} \geqslant \phi_{\rm aq} \geqslant \phi_{\rm qn}$ to enforce the time ordering of the four states. A given cell will have mass fractions $1 - \phi_{\rm fa}$ of fuel, $\phi_{\rm fa} - \phi_{\rm aq}$ of ash, $\phi_{\rm aq} - \phi_{\rm qn}$ of NSQE material, and $\phi_{\rm qn}$ of NSE material.

While a large portion of the energy release occurs in the consumption of ^{12}C, the final NSE state is not, during the explosion, energetically inert. The NSE state is one in which the distribution of nuclides in the fluid, and therefore the average nuclear binding energy, is determined by the fluid state. That is, it participates in the EoS of the fluid, releasing or absorbing energy as the pressure and density of the fluid change. As a result, a significant portion of the energy release for some fluid elements occurs well after the "fully burned" NSE state has been reached. The reaction kinetics used are given in Jackson et al. (2010). We track several material properties in the fully burned material, including the electron-to-baryon ratio (Y_e), ion-to-baryon ratio ($Y_{\rm ion}$), and average nuclear binding energy per baryon ($\overline{q}$).

Our treatment of matter in NSE allows for the effects of weak reactions, specifically electron captures, which serve to deleptonize the material. Weak processes (e.g., electron capture) are included in the calculation of the energy input rate, as are neutrino losses, which are calculated by convolving the NSE distribution with the weak interaction cross sections. Both the NSE state and the electron capture rates were calculated with a set of 443 nuclides (Seitenzahl et al. 2009b). Weak cross sections were taken from Fuller et al. (1985), Oda et al. (1994), and Langanke & Martínez-Pinedo (2001), with newer rates superseding earlier ones.

The treatment of electron capture is critical to the dynamics for three reasons. First, NSE is a dynamic equilibrium and the composition of material in NSE evolves as the thermodynamic state evolves and/or Y_e changes. Binding energy can be released if the equilibrium evolves toward more tightly bound nuclei, which changes the local temperature. Second, the reduction in Y_e lowers the Fermi energy, reducing the primary pressure support of this highly degenerate material and having an impact on the buoyancy of the neutronized material. Finally, neutrinos are emitted (since the star is transparent to them) so that some energy is lost from the system.

By using the progress variables defined above and the local Y_e, we can derive a local estimate for the abundance of ^{56}Ni. As was done in Townsley et al. (2009), we estimate the ^{56}Ni abundance by assuming that the first IGE material made as neutronization occurs is equal parts by mass ^{54}Fe and ^{58}Ni. The local mass fraction of ^{56}Ni is estimated by

$$Y_{e,n} = \frac{Y_e - (1 - \phi_{\rm qn}) Y_{e,f}}{\phi_{\rm qn}}$$
$$X_{^{56}\rm Ni} = \max\left[\phi_{\rm qn} \frac{Y_{e,n} - 0.48212}{0.5 - 0.48212}, 0\right], \quad (1)$$

where $Y_{e,f}$ is the electron fraction in the unburned fuel and 0.48212 is the electron fraction of material that is equal parts by mass ^{54}Fe and ^{58}Ni. This should be a modestly accurate estimate of the ^{56}Ni production because the dynamics of the progress variable $\phi_{\rm qn}$ have been calibrated to reproduce, in hydrodynamics, the production of IGEs during incomplete silicon burning seen in direct calculations (Zeldovich, Von Neumann, Döring; ZND; e.g., Khokhlov 1989) of steady-state detonations. When realization 2 from Jackson et al. (2010) with

$\rho_{\rm DDT} = 10^{7.1}$ g cm^{-3} is post-processed with a nuclear network, the ^{56}Ni yield from Equation (1) is within 2% of that determined by the post-processing. More detailed study of the accuracy of computed yields under various conditions is the subject of separate, ongoing work.

3.1.1. Deflagration

Even at our highest resolution (4 km), the flame front is unresolved. To handle this we use an artificial, resolved reaction front that is governed by the advection–diffusion–reaction (ADR) equation (Khokhlov 1995; Vladimirova et al. 2006), with special features to ensure that the front is stable and acoustically quiet (Townsley et al. 2007). Our ADR front is chosen to be resolved over about four computational cells in order to obtain acceptably low acoustic noise as it propagates across the grid and releases energy. This creates an extended "partially burned" region that requires some specialized treatment. In such regions, particularly at high density, we say that the material is well separated into unburned and fully burned material divided by a thin flame. However, the spatial resolution cannot capture this and the average over a mixture of fully burned and unburned results a "partially burned" state. Thus, we have to make estimates of the correct thermodynamic state of the two cases (unburned and fully burned) mixed together within the region.

Additionally, we enforce a minimum flame speed in order to prevent the flame from being torn apart by Rayleigh–Taylor-induced turbulence. The minimum flame speed is

$$S_{\rm min} = 0.5\sqrt{Agm\Delta}, \quad (2)$$

where A is the Atwood number, g is the local acceleration of gravity, Δ is the width of the grid cell, and m is an adjustable parameter, set to 0.04 for these simulations. The flame speed is set by

$$S = \max(S_{\rm min}, S_{\rm lam}). \quad (3)$$

The Atwood number and the laminar flame speed, $S_{\rm lam}$, are both functions of the local, unburned density estimate and the composition. The Atwood number varies by less than 0.01% due to the amount of ^{22}Ne present so it is tabulated for a representative, constant ^{22}Ne fraction.

3.1.2. DDT

At present, the physical mechanism by which a DDT in degenerate supernova material occurs is an area of current research (see Röpke 2007; Seitenzahl et al. 2009a; Woosley et al. 2009; Schmidt et al. 2010; Poludnenko et al. 2011, and references therein). Simulations of supernovae involving a DDT assume that it occurs via the Zeldovich-gradient mechanism (Khokhlov et al. 1997, but see also Niemeyer 1999), in which a gradient in reactivity leads to a series of explosions that are in phase with the velocity of a steadily propagating detonation wave. Many authors suggest that when the flame reaches a state of distributed burning, which is when turbulence on scales at or below the laminar flame width are fast enough to dominate transport processes (see, e.g., Pope 1987), fuel and ash are mixed and the temperature of the fuel is raised and "prepared" in such a way to produce the required reactivity gradient. A requirement for distributed burning is that the ratio of turbulent intensity to the laminar flame speed must exceed some unknown threshold, which is still actively researched (Niemeyer & Woosley 1997; Khokhlov et al. 1997; Golombek & Niemeyer 2005; Röpke & Hillebrandt 2005; Aspden et al. 2008, 2010; Poludnenko & Oran 2011a, 2011b). Entrance into the distributed burning regime does not guarantee such a reactivity gradient to form. Woosley (2007) and Woosley et al. (2009) studied incorporating more stringent requirements for these conditions to be met.

In the context of supernova models, the ratio of turbulent intensity to laminar flame speed changes most rapidly due to the change in laminar flame properties, which are strongly dependent on fuel density. Therefore, DDT is assumed to occur at a range of densities that vary somewhat but generally lie in the range of $10^{6.7}$–$10^{7.7}$ g cm^{-3} (Khokhlov et al. 1997; Lisewski et al. 2000; Woosley 2007; Röpke & Niemeyer 2007; Bravo & García-Senz 2008; Maeda et al. 2010; Jackson et al. 2010). We choose to ignite detonations where the flame reaches a specific density, $\rho_{\rm DDT} = 10^{7.1}$ g cm^{-3}, which puts us somewhere in the middle of that range, consistent with a number of studies on this subject. We note that while parameterizing the DDT criteria by only density omits effects such as background turbulent intensity and density gradients, our choice of one threshold is intended to keep such variables constant so that we can isolate and investigate the effect of varying the central density.

The choice of $\rho_{\rm DDT}$ increases or decreases the duration of the deflagration phase, which increases or decreases the amount of expansion prior to the detonation and hence the yield of IGEs. A companion study of the effects of varying $\rho_{\rm DDT}$ as a proxy for metallicity under the same statistical ensemble we use here indicated a slight overproduction of ^{56}Ni at this choice of $\rho_{\rm DDT}$ (Jackson et al. 2010), a result borne out by this study. The DDT transition is implemented by burning small regions ahead of rising plumes. When a plume reaches $\rho_{\rm DDT}$, a circular region with a radius of 12 km is selected 32 km radially outward from the point where the rising plume reaches the transition density. The reaction progress variables in this region are then instantly increased to a fully burned state. This method conserves energy, as the detonation is initiated by the sudden release of energy from the conversion of fuel to NSE, not by an unphysical addition of extra energy. Each plume is limited to ignite no more than two to three detonations, with a minimum separation distance of 200 km imposed between detonation points. The full details of this algorithm are given in Section 3.2 of Jackson et al. (2010).

Previous studies using this DDT mechanism found that DDT points with a 12 km radius successfully generated detonations in all simulations performed. However, our simulations showed that this size DDT point is not as robust for this study. One of our simulations ($\rho_{c,0} = 1.0 \times 10^9$ g cm^{-3}, realization 8) deviated from the behavior of the other 149 simulations and inspection showed that the first plume to reach $\rho_{\rm DDT}$ ignited several DDT points that did not propagate as detonations; the first detonation to actually propagate ignited when the second plume reached $\rho_{\rm DDT}$ significantly after (and beneath) the first plume to reach $\rho_{\rm DDT}$. The failure of the detonation of the first plume to reach $\rho_{\rm DDT}$ led to significantly more expansion of the WD prior to the subsequent detonation, which led to some or all of the material burning at a lower density than it should have, and the corresponding suspect yields. Thus, we removed this simulation from our suite and performed the analysis on the remaining 149 points. Even if this "failed DDT" simulation is included, the results presented in this paper change by no more than a few percent.

3.2. Mesh Refinement

Refinement is based on gradients in ρ and $\phi_{\rm fa}$, subject to the limits imposed below. We define three types of regions, subject to different refinement limits:

1. fluff (f): regions with $\rho < \rho_{\rm fluff}$;
2. star (*): non-energy-generating stellar material, $\rho > \rho_{\rm fluff}$;
3. energy generation (eg):
   regions with $\epsilon_{\rm nuc} > \epsilon_{\rm eg}$ or $\dot{\phi}_{\rm fa} > \dot{\phi}_{\rm fa,eg}$,

where $\phi_{\rm fa}$ is the reaction progress variable from the ADR equation, and $\epsilon_{\rm eg}$ and $\dot{\phi}_{\rm fa,eg}$ are parameters equal to 10^{18} erg g^{-1} s^{-1} and 0.2 s^{-1}, respectively. These limits are chosen so that all actively propagating flames or detonation fronts are at the highest resolution. We establish a minimum cell size for refinement of each type of region such that $\Delta_f > \Delta_* > \Delta_{\rm eg}$. We use $\Delta_{\rm eg} = 4$ km and $\Delta_* = 16$ km, and allow Δ_f to be as large as allowable. FLASH only allows adjacent sub-domains of the mesh to be of fixed size (we use 16×16 cells) and to differ by a single refinement level (a factor of two in resolution). These were found to be the lowest resolutions that gave converged results in one-dimensional (1D) simulations (Townsley et al. 2009).

Fluff is the low-density area outside of the star; we choose $\rho_{\rm fluff} = 10^3$ g cm^{-3}. The FLASH code cannot properly handle empty (zero-density) regions, so these regions are set to some low, but non-zero, density so that they will not affect the dynamics of the star. To avoid rapidly cycling the refinement–derefinement of a region, a small amount of hysteresis is introduced near the limits for refinement changes, so that, for example, a refinement of grid resolution is not immediately derefined as a result of slight changes due to the necessary interpolation.

4. RESULTS

The results presented here build on the initial results presented in Krueger et al. (2010) and extend the analysis beyond what was shown there. The explosions occur in two main phases, the deflagration phase (from ignition until the first DDT occurs) and the subsequent detonation phase. The principal difference is that during the deflagration phase, the star has time to react to the energy release. Accordingly, the evolution is naturally divided by the time at which the first DDT event occurs, which we define as $t_{\rm DDT}$; this duration also describes the time spent in the deflagration-dominated phase of the SN Ia evolution. We also define $t_{\rm IGE}$ as the time when the production of IGEs ceases. This is the time at which burning ceases, and by this time the NSE state is no longer evolving due to freezeout; thus, energy release has effectively ceased by $t_{\rm IGE}$. However, our models have not yet entered into free expansion by this time. For the purpose of our simulations, $t_{\rm IGE}$ also measures the duration of the entire SN Ia event. We found that the duration of the deflagration phase ($t_{\rm DDT}$) decreases with increasing density and is less sensitive to density as the density increases, while the duration of the detonation phase (equal to $t_{\rm IGE} - t_{\rm DDT}$) is very nearly constant for all simulations, with a mean of 0.476 s and a standard deviation of 0.065 s.

Table 7 in Appendix C presents the masses of ^{56}Ni and IGEs at $t_{\rm DDT}$ and $t_{\rm IGE}$. Recall from Table 1 that the total mass and the mass of the convective core both change with density, but the variations are only of a few percent. Thus, we believe that effects from variations in the total or convective core masses are negligible. The results and trends we describe follow from variations in the central density and the variations in initial conditions from realization to realization. Also, as discussed in Section 3 of Krueger et al. (2010), the choice of the DDT transition density in our simulations led to an overproduction of ^{56}Ni. Essentially, our models are systematically too bright, but we believe that our trends are valid. Jackson et al. (2010) investigated the role of DDT density in our models and found that the production of ^{56}Ni is very sensitive to the choice of DDT density. This choice determines the duration of the deflagration phase, which determines the amount of expansion and, accordingly, the density profile of the star during the detonation and the yield. Future studies will be better calibrated based on these results.

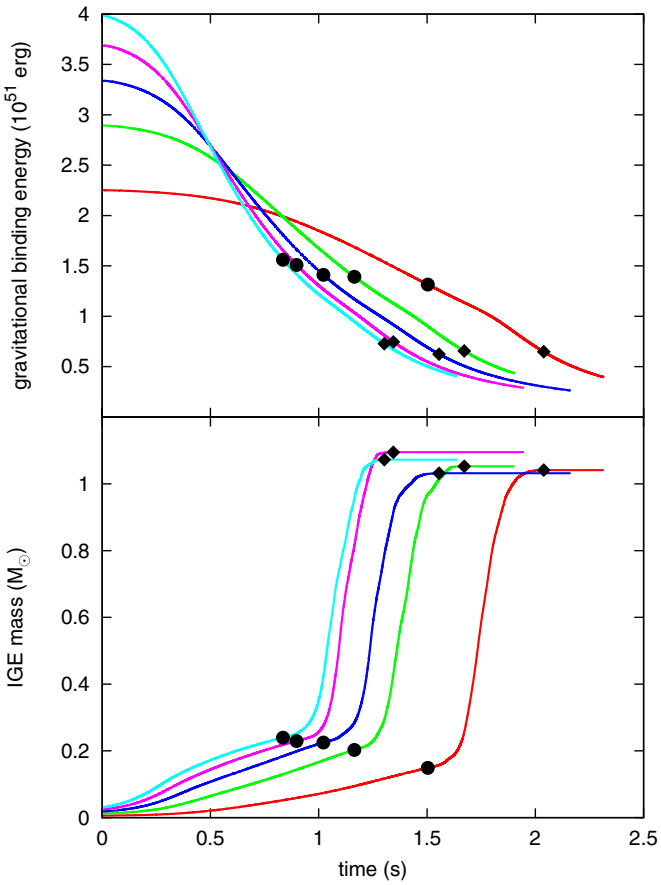

Figure 3. Sample curves showing the evolution of the gravitational binding energy and the mass of IGEs over the duration of a simulation. These curves all use realization 5. Curves are colored by $\rho_{c,0}$: 1.0×10^9 g cm^{-3} (red), 2.0×10^9 g cm^{-3} (green), 3.0×10^9 g cm^{-3} (blue), 4.0×10^9 g cm^{-3} (magenta), and 5.0×10^9 g cm^{-3} (cyan). The times $t_{\rm DDT}$ and $t_{\rm IGE}$ are marked by black circles and black diamonds, respectively.

(A color version of this figure is available in the online journal.)

4.1. Evolution

Figure 3 shows the evolution of the gravitational binding energy and the mass of IGEs for the five simulations performed using realization 5, each with a different $\rho_{c,0}$. During the deflagration-dominated phase, higher $\rho_{c,0}$ progenitors experience faster burning, thus expanding the star faster due to the faster energy release. This effect can be seen by the rapid drop of the binding energy for the higher density simulations around 0.5 s in the upper panel. The transition to a detonation in higher $\rho_{c,0}$ progenitors occurs sooner. Once the first DDT event occurs, the production of IGEs proceeds much faster than in the deflagration phase, as may be seen by the sudden increase of the slope in the lower panel after the detonation occurs.

During the detonation phase the drop in binding energy is similar for all densities. During this same period the curves of the IGE mass stay ordered, with the differences between them following principally from the difference in $t_{\rm DDT}$. The nonlinear

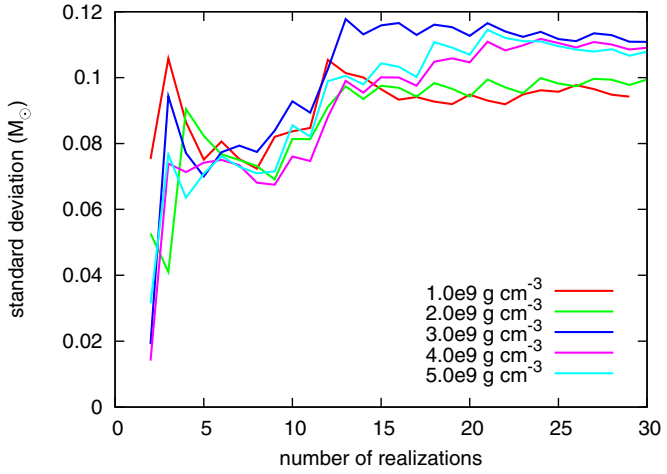

Figure 4. Plot of the standard deviation of ^{56}Ni yield as a function of the number of realizations, added in the order listed in Appendix A, for each of the five central densities of the study. The standard deviation of the ^{56}Ni mass converges around 15 total realizations.

(A color version of this figure is available in the online journal.)

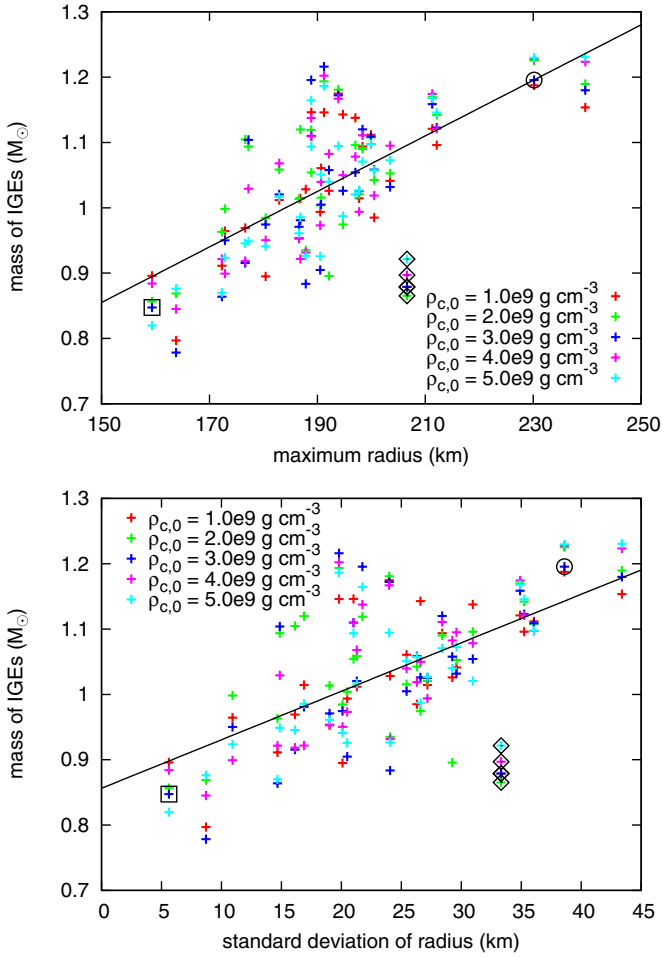

Figure 5. Plots of the mass of IGEs as functions of the maximum initial flame radius and the standard deviation of the initial flame radius, both being treated as measures of how spiky the initial flame surface is, with simulations colored by $\rho_{c,0}$. The black square marks realization 10 and the black circle marks realization 21, both with $\rho_{c,0} = 3 \times 10^9$ g cm^{-3}. These two simulations are shown in Figures 2(a)– (d), and are examples of extreme cases: very smooth (realization 10) and very spiky (realization 21). Black diamonds mark realization 24, an example that runs counter to the general trend, and a good illustration of the ambiguity of the intermediate regions of these plots.

(A color version of this figure is available in the online journal.)

morphological dependencies come into play as the detonation slows and then stops; the total IGE yield plateaus to a constant value, but that value is not (for a single realization) correlated with the central density of the progenitor. The leveling off of the mass of IGEs, due to the cessation of burning, is apparent in the lower panel. The time $t_{\rm IGE}$ was calculated for each simulation by finding the point at which the IGE mass changes by less than 0.01% over the preceding 0.01 s.

4.2. Statistics

We showed in Krueger et al. (2010, see especially Figure 2) that a single initial morphology is, in general, insufficient to capture trends in SNe Ia due to the nonlinearities involved in the explosion process. This observation invites the question of how many initial morphologies are necessary to obtain statistically meaningful trends from the simulations. Figure 4 presents the standard deviation of ^{56}Ni yield as a function of the number of realizations, with the realizations added in the order presented in Appendix A. Shown are the standard deviations for each of the five central densities of the study. The obvious evolution of the standard deviation until approximately 15 realizations are included in the average shows that a statistically meaningful average requires approximately 15 realizations. From this result, we conclude that our sample of 30 realizations per central density is sufficient to fully characterize the statistical trends we present. The choice of 30 realizations allows us to go somewhat beyond characterizing the variation in the sample, allowing us to reduce our uncertainty on the sample mean.

This result, the need for an average over an ensemble of simulations for determining statistically meaningful trends, is critical to the analysis of our study. Because the results discussed in this paper come from a statistical analysis of our simulations, the results presented here generally cannot be applied predictively to individual SNe Ia, but only apply statistically to large sets of SNe Ia. Exceptions to this rule will be noted explicitly.

4.3. Initial Morphology Correlations

We explored whether properties of the initial flame morphology correlate with the final result. We find that "spikier" initial flame surfaces, that is initial morphologies that appear to have a small number of large amplitude perturbations, give rise to faster plume growth and less expansion, and, therefore, a higher yield of IGEs and ^{56}Ni. Several quantities were tested as measures of the morphology of "spikiness," and each gave the same qualitative result. For example, Figure 5 plots the final yield of IGEs as a function of the maximum radius of the initial flame surface and standard deviation of the initial flame radius.

As illustrative cases, consider Figure 2. The right panels show realization 10, $\rho_{c,0} = 3 \times 10^9$ g cm^{-3}, which is a very smooth initial flame surface; this same realization is outlined by a black square in Figure 5. The smooth configuration results in several rising plumes approaching $\rho_{\rm DDT}$, and these multiple plumes burn a larger fraction of the star and release more energy than a single plume would during its rise to $\rho_{\rm DDT}$. The net effect is an increase in both $t_{\rm DDT}$ and in the amount of expansion at $t_{\rm DDT}$, leaving less mass at densities high enough to burn to IGEs during the detonation phase. Contrast this with the left panels of Figure 2, showing realization 21, $\rho_{c,0} = 3 \times 10^9$ g cm^{-3}, which is a very spiky initial flame surface; this same realization is outlined by a

black circle in Figure 5. For this case, a single plume is dominant over all other features of the initial flame surface and rapidly accelerates toward $\rho_{\rm DDT}$ with little competition. This gives a short deflagration phase, and burns a lower fraction of the star prior to the detonation (see especially Figure 2(c)). These two effects result in less expansion at $t_{\rm DDT}$, leaving more mass at a density high enough to burn to IGEs during the detonation, resulting in a greater yield of IGEs and ^{56}Ni.

In the center of each panel of Figure 5, the trend is not so clear. Realization 24 (outlined by black diamonds) is a good example of the lack of a clear trend in this intermediate range. The initial flame surface for realization 24 has multiple large spikes, so that it has a larger than average maximum radius and radial standard deviation, and would be considered a spiky case. However, most of these spikes are of comparable maximum radius, and none of these features develops into a dominant plume, as is typical of the spiky cases; instead, the plumes grow together and the behavior is like that of the smooth cases. Thus, realization 24 leads to high values of $t_{\rm DDT}$ and low yields of IGEs and ^{56}Ni relative to simulations of similar spikiness. Thus, the intermediate range does not show a strong trend, while the extreme ranges (multiple competing plumes starting from a smooth initial surface, or a single dominant plume with no significant competition) show the trend more clearly.

4.4. Yields

Figure 6 shows the masses of IGEs and ^{56}Ni produced in the 149 simulations that were analyzed, along with the ^{56}Ni-to-IGE mass ratio. The figures plot yield versus central density and also show average yields and standard deviations at each central density, with best-fit trend lines. The mass of IGEs is consistent with a flat line; i.e., it is independent of $\rho_{c,0}$. However, the mass of ^{56}Ni decreases with increasing $\rho_{c,0}$. The significant scatter in the two masses is readily apparent; the mean standard deviations for the IGEs and ^{56}Ni masses are 0.108 $M_\odot$ and 0.105 $M_\odot$, respectively. As discussed in Mazzali & Podsiadlowski (2006) and Woosley et al. (2007), assuming a constant IGE mass and varying the ^{56}Ni mass produces SNe Ia that lie approximately along the observed width–luminosity relationship, while the width of the relationship allows the IGE mass to vary somewhat (cf. Figures 15 and 20 of Woosley et al. 2007). We note that the masses of IGEs and in particular the masses of ^{56}Ni from our simulations are on average higher than accepted results for masses synthesized in actual SN Ia events (see Woosley et al. 2007, and references therein).

The ^{56}Ni-to-IGE mass ratio decreases with increasing $\rho_{c,0}$, as would be expected from a constant IGE mass and a decreasing mass of ^{56}Ni. However, unlike the constant standard deviations of these two masses, the standard deviation of the ^{56}Ni-to-IGE mass ratio increases with $\rho_{c,0}$. The variation in the ^{56}Ni-to-IGE ratio is dominated by variation related to neutronization: Because neutronization can exaggerate differences that arise in the hydrodynamics, we find that the standard deviation (variation) increases with the total mass of stable IGEs synthesized.

Additionally, we found that the yield from burning during the deflagration phase is substantially different from the yield during the detonation phase. Figure 7 shows the yields of stable IGEs and ^{56}Ni during the deflagration and detonation phases. The trend of increasing stable IGE yield and decreasing ^{56}Ni yield with increasing central density is most obvious in the deflagration phase yield. We interpret this result as following from the fact that the detonation phase involves burning at densities that are typically lower than those of the deflagration

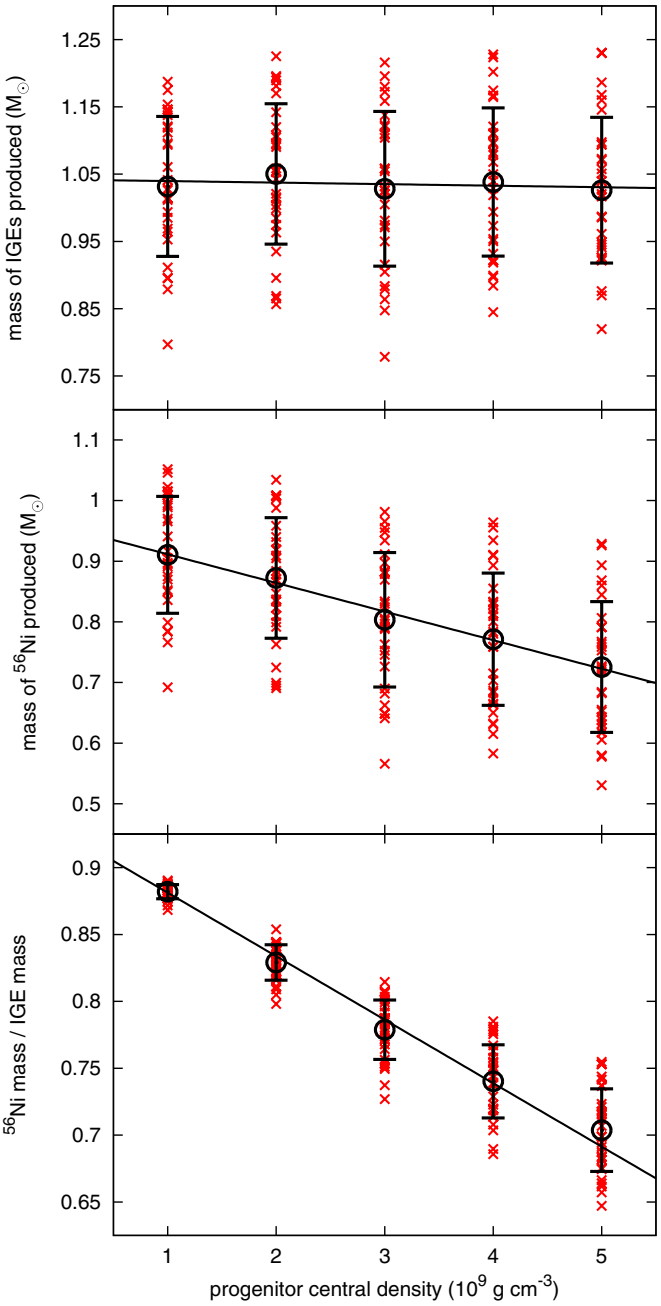

Figure 6. Final yields (at $t_{\rm IGE}$) of our simulations plotted against $\rho_{c,0}$. The black lines are the best-fit trend lines, with the averages and standard deviations marked by the circles and the vertical error bars.

(A color version of this figure is available in the online journal.)

phase due to expansion of the star during the deflagration phase. The neutronization rate increases with density, so it shows up most strongly in the deflagration phase before significant expansion occurs.

4.5. Distribution of ^{56}Ni

The principal result from a simulation is the mass of ^{56}Ni synthesized in the explosion, which directly sets the brightness of an event. The synthesized ^{56}Ni masses are listed in Appendix C. The next question to be answered in the analysis concerns the distribution of ^{56}Ni in the remnant. Figure 8 presents radially averaged profiles of ^{56}Ni for three of the five central densities ($\rho_{c,0} = 1 \times 10^9$, 3×10^9, and 5×10^9). Also shown are representative results from realizations 4, 12, 13, and 29 for comparison.

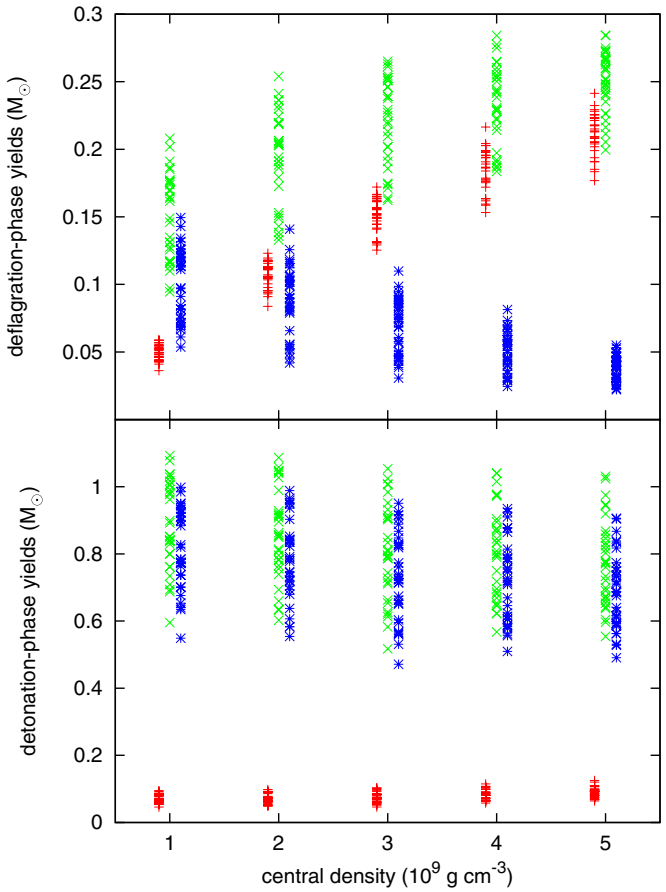

Figure 7. Plots of the masses of stable IGEs (red pluses), ^{56}Ni (blue asterisks), and total IGEs (green crosses) produced during the deflagration phase (top panel) and the detonation phase (bottom panel). The symbols for each mass have been horizontally shifted slightly so that the symbols do not overlap.

(A color version of this figure is available in the online journal.)

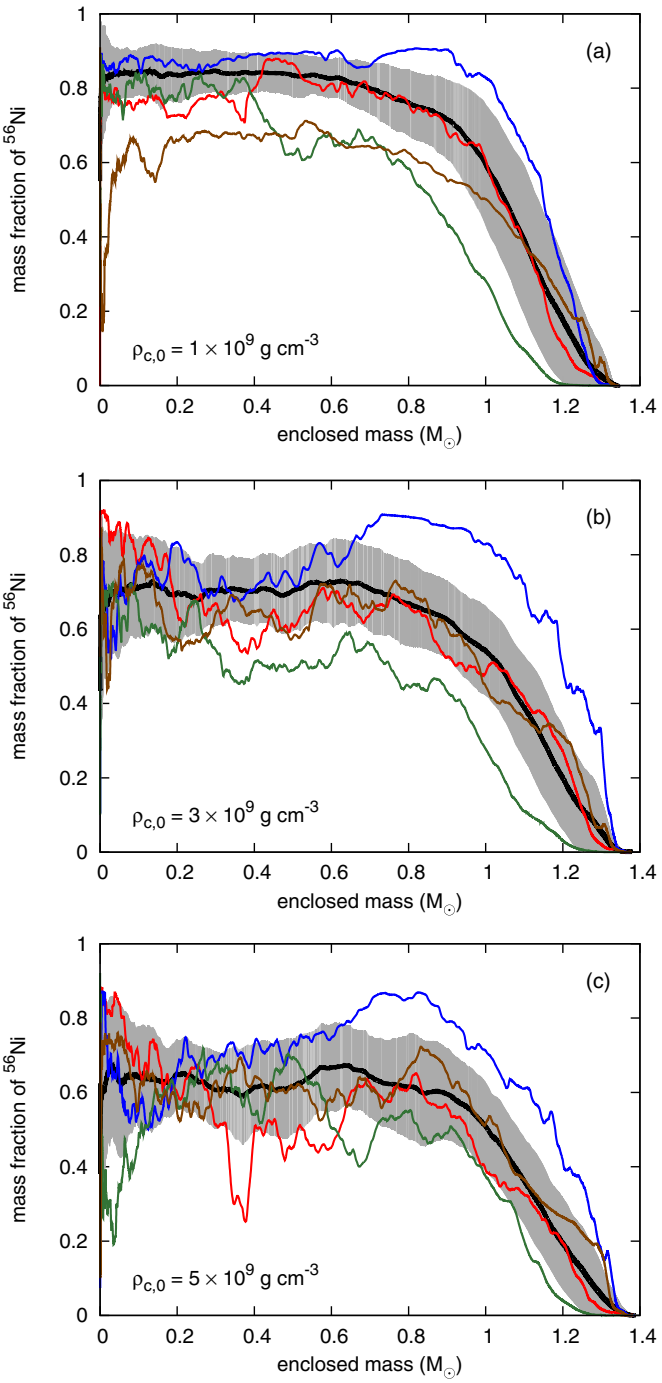

Figure 8. Radially averaged profiles of ^{56}Ni mass fraction at three central densities (1×10^9, 3×10^9, and 5×10^9 g cm^{-3} in panels (a), (b), and (c), respectively). The black curves show the mean profile of all simulations at a given $\rho_{c,0}$, with the gray band showing the standard deviation. The four colored curves represent four different realizations: 4 (red), 12 (blue), 13 (green), and 29 (brown).

(A color version of this figure is available in the online journal.)

The radial profile of ^{56}Ni mass fraction varies between simulations, but certain details are consistent across the ensemble. The inner 0.8–1.0 $M_\odot$ has a high ^{56}Ni mass fraction; we refer to this region as the "plateau," although there can be significant variation within this region. Outside of the plateau, there is a smooth decrease to a ^{56}Ni mass fraction at or near zero at the surface of the WD; we refer to this as the "decline" region. It appears that this decline region may not be fully relaxed to the final profile at time $t_{\rm IGE}$, but may experience some steepening prior to entering the free-expansion phase. Lower $\rho_{c,0}$ simulations have less neutronization and therefore generate more ^{56}Ni. For these simulations the ^{56}Ni mass fraction in the plateau tends to cluster near the maximum value (∼0.9), with some deviations down as far as ∼0.6. The higher $\rho_{c,0}$ simulations have more neutronization and therefore generate less ^{56}Ni, so the typical ^{56}Ni mass fraction in the plateau shows more variation and there exist larger deviations from the mean (down to ∼0.2).

The representative realizations presented in Figure 8 demonstrate the deviation from mean behavior. In particular, the representative realizations show "typical" behavior (the ^{56}Ni profile nearly matches the mean profile), overluminous and underluminous models, and ^{56}Ni holes (patches within the plateau with significantly less ^{56}Ni than the surrounding regions). Previous studies have reported the presence of a ^{56}Ni hole in the inner region (Höflich et al. 2010). The green and red curves in the bottom panel of Figure 8 (realization 4) illustrate such a ^{56}Ni deficit, although the deficit is offset from the center of the WD in the case of the red curve. Most of our simulations do not show evidence of this ^{56}Ni hole in the inner region. Only a few simulations have such a feature, with ^{56}Ni holes being more common in simulations with a higher $\rho_{c,0}$. Turbulent mixing caused by the burning processes breaks the symmetries that give rise to a consistent central ^{56}Ni hole in 1D simulations.

Figure 9 shows the distributions of ^{56}Ni, stable IGEs, and non-IGE material for the four sample cases shown in Figure 8(c)

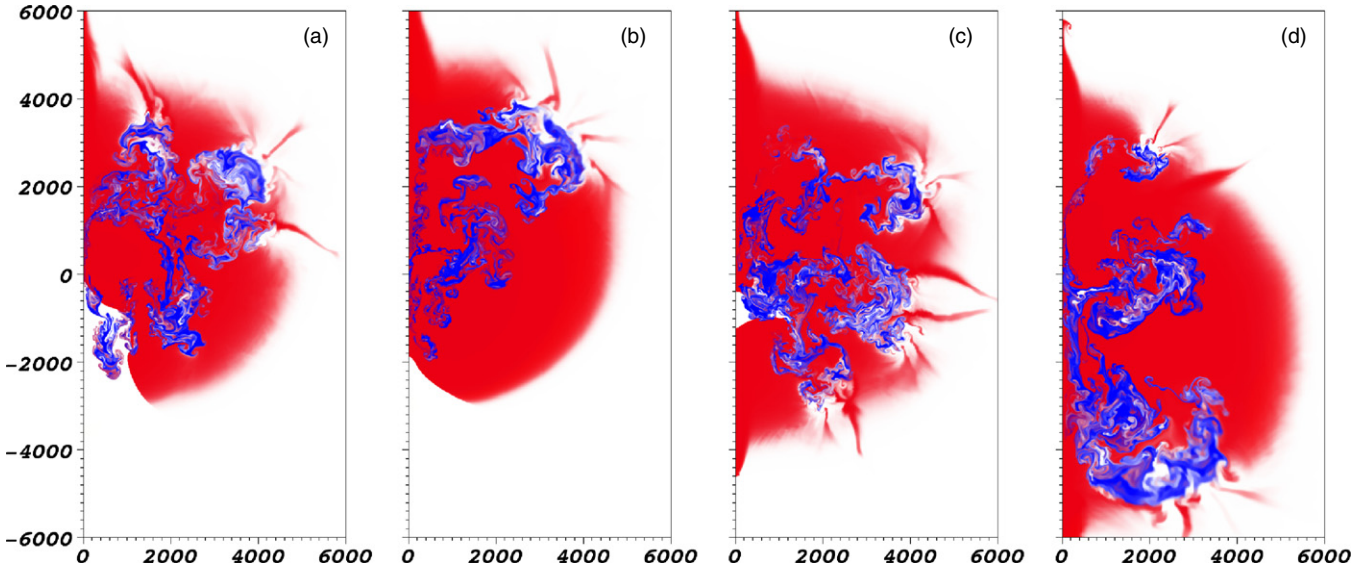

Figure 9. Plots of the inner 6000 km of four simulations at $t_{\rm IGE}$, showing mass fractions of ^{56}Ni (red), stable IGEs (blue), and non-IGE material (white). These are the same simulations plotted in Figure 8(c), with $\rho_{c,0} = 5 \times 10^9$ g cm^{-3}; from left to right, the panels show a non-central ^{56}Ni hole (realization 4), an overluminous case (realization 12), an underluminous case with a central ^{56}Ni hole (realization 13), and a typical case (realization 29). The off-center ^{56}Ni deficit in realization 4 is due to a band of neutronized, stable isotopes caused by multiple plumes that have reached a common radius. The central ^{56}Ni hole in realization 13 is partially due to a neutronized region around the equator, and partially due to an incompletely burned region near the axis, below the equator.

(A color version of this figure is available in the online journal.)

($\rho_{c,0} = 5 \times 10^9$). For our results, the mass of stable IGEs is approximated by any IGE material that is not ^{56}Ni. The figures present the inner 6000 km of the domain, and for all cases the bulk of IGEs appears in the plotted region. The distributions indicate that ^{56}Ni holes can be caused by incompletely burned regions (for example, on the axis of Figure 9(c) just below the equator) or by neutronized regions (for example, adjoining the previously mentioned incompletely burned region of Figure 9(c), or the band at a radius of ∼2000 km in Figure 9(a)). The plume rise, velocity fields, and neutronization may be asymmetric, which is seen especially in Figures 9(a) and (d). The degree of asymmetry observed in our models suggests that there may be noticeable line-of-sight effects for SNe Ia.

4.6. Distinguishing Age among SNe Ia of Equal Brightness

Can we extract from our results insight into the age of a progenitor WD given the brightness of the SN Ia? From our results, one might conclude that the mass of stable IGEs ($M_{\rm stable}$) should increase with increasing $\rho_{c,0}$, and that the relation should have a large scatter (akin to the scatter in the ^{56}Ni and IGE relations). Figure 10 illustrates the relationship between $\rho_{c,0}$ and $M_{\rm stable}$, along with the best-fit trend and the scatter (the shaded region shows two standard deviations in each direction around the best-fit curve through the data). The data show an increasing trend as expected, with the best fit being

$$\left(\frac{\rho_{c,0}}{10^9\ {\rm g\ cm^{-3}}}\right) = 35.4\left(\frac{M_{\rm stable}}{M_\odot}\right)^2 + 6.92\left(\frac{M_{\rm stable}}{M_\odot}\right) - 0.349. \quad (4)$$

Unlike the ^{56}Ni and IGE relations, however, there is a very small scatter in this relation for $M_{\rm stable}$, with a standard deviation of only 0.167×10^9 g cm^{-3}. This result is the tightest relation in our data, to the point where this relation can be meaningfully applied to a single event. This tight relationship is unlike all of our other relations, which only apply to the statistics of large ensembles.

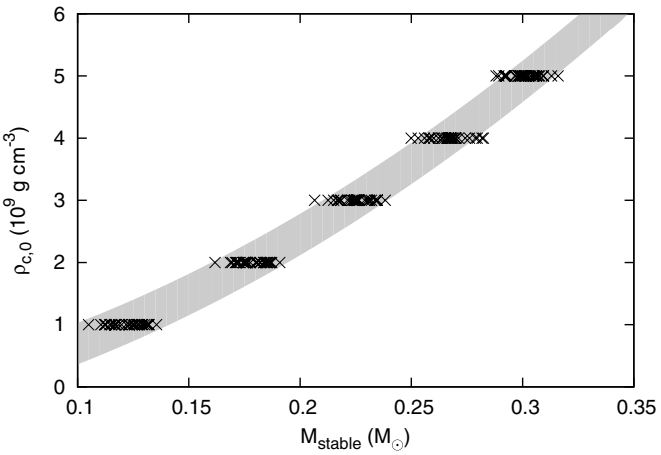

Figure 10. Plot of $\rho_{c,0}$ vs. $M_{\rm stable}$. The shaded region displays two standard deviations around the model (Equation (4)).

Given observations of multiple SNe Ia of the same brightness and a reliable measure of the mass of stable IGEs from the observations, our models predict that we can use Equation (4) to determine the relative ages of the progenitors. The relation provides the central density from observed masses of stable IGEs. Lesaffre et al. (2006) present relations between the cooling time of the progenitor and the central density of the progenitor at the ignition of the thermonuclear runaway. Applying the relations of Lesaffre et al. (2006) to the central densities, our result allows determination of the cooling times the progenitor WDs experienced. Assuming the progenitors had the same main-sequence mass, we thus obtain a measure of the relative ages of the progenitors. Because this result is

derived from varying the central density of the progenitor, we are implicitly assuming that such a variation of $\rho_{c,0}$ is the dominant effect on the mass of stable IGEs. Future work in 3D will consider central density variation combined with other effects that may be related to age.

Our models, specifically the distribution of IGEs in the expanding remnant, offer insight into what would be required for observing the mass of stable IGEs. While our models exhibit a mild degree of asymmetry, we find systematic behavior of the distribution of heavy nuclei for events of a given brightness (or given mass of ^{56}Ni). Figure 11 shows profiles of ^{56}Ni and IGE mass fractions in three sets. Each set has a simulation at each of the five central densities, but the simulations within a set are chosen to have approximately the same integrated ^{56}Ni mass. Accordingly, the simulations within a set may not be from the same realization. These profiles are generated at $t_{\rm IGE}$, when the burning has essentially ceased, but not yet into the free-expansion phase.

The plateau (central region) exhibits a slight systematic behavior in Figure 11. Considering both the curves of ^{56}Ni and IGEs, we note a tendency of a less well-defined plateau in the lowest ^{56}Ni-mass set (top panel). The start of the decline region occurs at a higher enclosed mass for simulations with a higher mass of ^{56}Ni; the plateau extends farther out. Also, there appears to be a mild trend in the plateau region of simulations within a set: The higher $\rho_{c,0}$ simulations (magenta and cyan curves) tend to show a wider plateau in the IGE mass fraction. In addition, we note that within these results, some simulations exhibit the ^{56}Ni hole while some do not. The hole may be observed in the drastic decrease of some curves at the lowest enclosed masses.

We may also consider the distribution of the synthesized heavy elements within the models. Figure 12 shows the distribution of ^{56}Ni versus stable IGEs for three of the simulations from Figure 11(a). The densities of the three simulations ($\rho_{c,0} = 1 \times 10^9$, 3×10^9, and 5×10^9 g cm^{-3}) span the range of central density. The trend for more stable IGEs at higher $\rho_{c,0}$ can clearly be seen by the more extensive regions colored in blue, indicating higher mass fractions of stable IGEs. These 2D plots also show that as $\rho_{c,0}$ increases, the ^{56}Ni and stable IGEs are more sharply segregated; there are more mixed regions (in shades of purple) in the lowest $\rho_{c,0}$ simulation (Figure 12(a)).

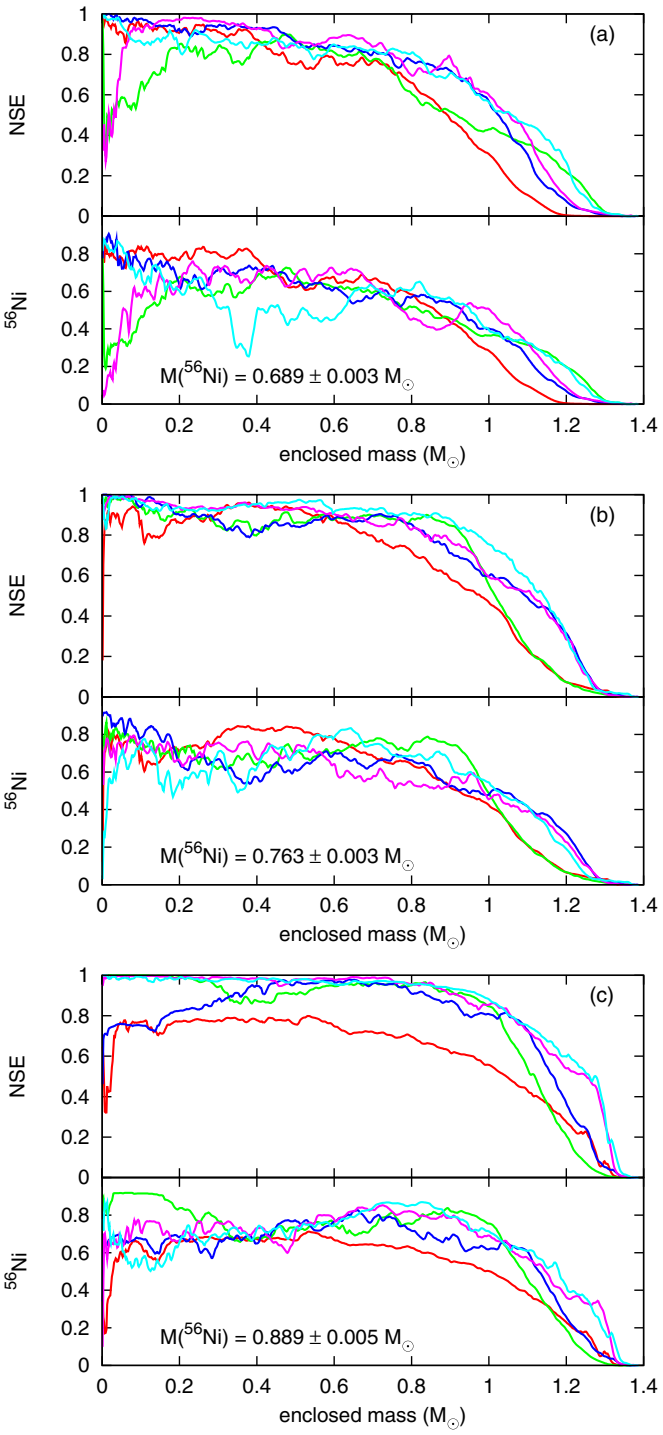

Figure 11. Comparisons of radial profiles of ^{56}Ni and IGE mass fractions for models with nearly the same total mass of ^{56}Ni, but different values of $\rho_{c,0}$. The upper set of profiles has a mass of $0.689 \pm 0.003\ M_\odot$, the central set of profiles has a mass of $0.763 \pm 0.003\ M_\odot$, and the lower set of profiles has a mass of $0.889 \pm 0.005\ M_\odot$. Lines are colored by $\rho_{c,0}$: 1.0×10^9 g cm^{-3} (red), 2.0×10^9 g cm^{-3} (green), 3.0×10^9 g cm^{-3} (blue), 4.0×10^9 g cm^{-3} (magenta), and 5.0×10^9 g cm^{-3} (cyan).

(A color version of this figure is available in the online journal.)

5. DISCUSSION

The results presented in Section 4 follow directly from our simulations and are as rigorous as can be within the limitations of our models (as described in Section 2). We may extend our results in order to investigate the implications of our trends, particularly the decreasing proportion of ^{56}Ni with increasing central density. The principle result from one of our simulations is the mass of ^{56}Ni, and there are well-established relationships between the brightness of an observed thermonuclear supernova and the mass of ^{56}Ni synthesized during the explosion (see Woosley et al. 2007, and references therein). Thus, our trends may have implications for the brightness of events. In this section, we explore these connections by comparing our trends in ^{56}Ni mass to ^{56}Ni masses inferred from observations.

In Krueger et al. (2010, see especially their Figure 4, an updated version of which is shown in Figure 14 of this paper), we showed that our results agree with the general trend of dimmer SNe Ia from older stellar populations by comparing with observations from Neill et al. (2009). We improve upon that result with two additions: recalibration of the ^{56}Ni mass produced by our models and clarifying the definition of "age" by including a range of main-sequence lifetimes. Additionally, this section discusses how our results compare to other studies considering the effect of $\rho_{c,0}$ on ^{56}Ni.

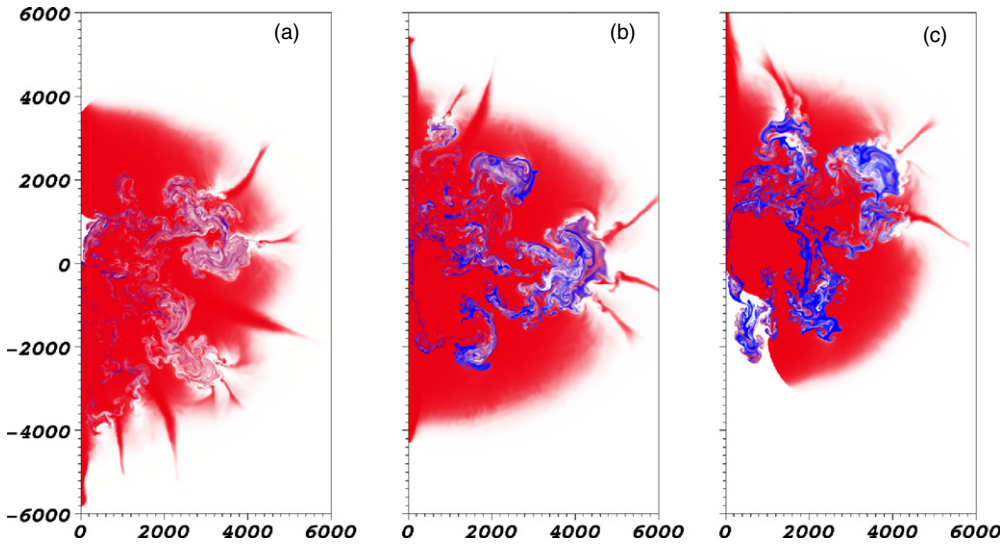

Figure 12. Comparison of ^{56}Ni and stable IGE distributions at t_{IGE} for simulations with the same total ^{56}Ni mass. These images are generated from the same simulations used in Figure 11(a). From left to right, the central densities are 1.0, 3.0, and 5.0 $\times 10^9$ g cm^{-3}. Red represents the mass fraction of ^{56}Ni, blue represents stable IGEs, and white represents non-IGEs. Axes are in kilometers. As $\rho_{c,0}$ increases (with constant ^{56}Ni), more IGEs are produced and less material is mixed (seen by the purple regions).

(A color version of this figure is available in the online journal.)

5.1. Recalibration of ^{56}Ni Yield

As discussed above, on average our suite of simulations exhibited an overproduction of IGEs and ^{56}Ni when compared with masses estimated from observations of remnants (Woosley et al. 2007). We estimate a correction to our ^{56}Ni masses (the details of which are given in Appendix B but which we summarize here) that allows us to more directly compare our results to ^{56}Ni masses inferred from observations.

The recalibration is based on relationships between model parameters and explosion yields found in previous studies. Jackson et al. (2010) found that higher values of ρ_{DDT} led to increased yields due to less expansion of the star during the deflagration phase. Townsley et al. (2009) found a correspondence between the mass at densities above 2×10^7 g cm^{-3} at t_{DDT} and the mass of IGEs synthesized in the yield (Figure 5). Although the correspondence found by Townsley et al. (2009) was not perfect, these two relationships form the basis for our rescaling. We note that the rescaling assumes that even for lower values of ρ_{DDT}, the mass of IGEs is independent of $\rho_{c,0}$; this assumption is discussed in greater detail in Appendix B based on the expansion characteristics present in our simulations. However, this is a critical assumption in our analysis and is based on a somewhat restricted parameter space and therefore is subject to future investigation to confirm it. Recent work by Seitenzahl et al. (2011), who performed full 3D simulations covering the range of observed ^{56}Ni masses, suggests that this assumption does not hold (see Section 5.3).

Performing this recalibration lowers the ^{56}Ni masses (see Figure 13), giving yields that are consistent with yields inferred from observations. A similar trend of decreasing ^{56}Ni mass with increasing central density is also found in these extrapolated results. Future models will extend to three dimensions and may include more physically motivated initial conditions or more detailed burning models that capture interactions between the turbulent velocity field and the flame structure. Such changes will require that we re-evaluate our choice of model parameters, such as ρ_{DDT}.

5.2. Comparison to Observations

One of the principal metrics that we extract from each simulation is the mass of ^{56}Ni produced, which is directly related to the brightness of an event. Using the method outlined in Howell et al. (2009), we converted stretch reported in observational results to ^{56}Ni masses to compare to the ^{56}Ni masses (derived in Section 5.1) obtained from our simulations. We then combined our central density values with the results of Lesaffre et al. (2006), which correlate the central density at the time of the ignition of the flame front to the cooling time of the progenitor WD, allowing us to express our results as ages. The results of Lesaffre et al. (2006) suggest that a WD with a central density of 1×10^9 g cm^{-3} will not ignite without further accretion, so for this comparison we neglect our simulations with that value of $\rho_{c,0}$. Our "age" was previously defined as the delay time (τ_{cool}), while the observational results used the delay time, which includes the main-sequence lifetime (τ_{MS}). We can improve our comparison by applying a shift to our data to account for τ_{MS}. We assume that our progenitors differ solely in their cooling times in order to separate out other effects; therefore, we take τ_{MS} to be constant across our results. Our best-fit line would now become

$$M_{^{56}\mathrm{Ni}} = \alpha \log_{10}(\tau_{cool} + \tau_{MS}) + \beta, \quad (5)$$

where α and β are fitting parameters. Because the addition of τ_{MS} is inside the logarithm, this corresponds not only to a shift but also an increasing slope. We have selected two estimated limiting values for τ_{MS} (0.05 and 1.0 Gyr, corresponding to main-sequence masses of approximately 8.0 and 1.5 $M_\odot$, respectively; see Hansen et al. 2004) and included them with the original $\tau_{MS} = 0$ result in Figure 14. Adding in a τ_{MS} consistent with our C/O progenitors brings our results into better agreement with the two rightmost points of Neill et al. (2009).

As seen in Figure 14, our theoretical results are not in complete agreement with the observed data. Observationally, the age–brightness correlation may flatten at young ages, while

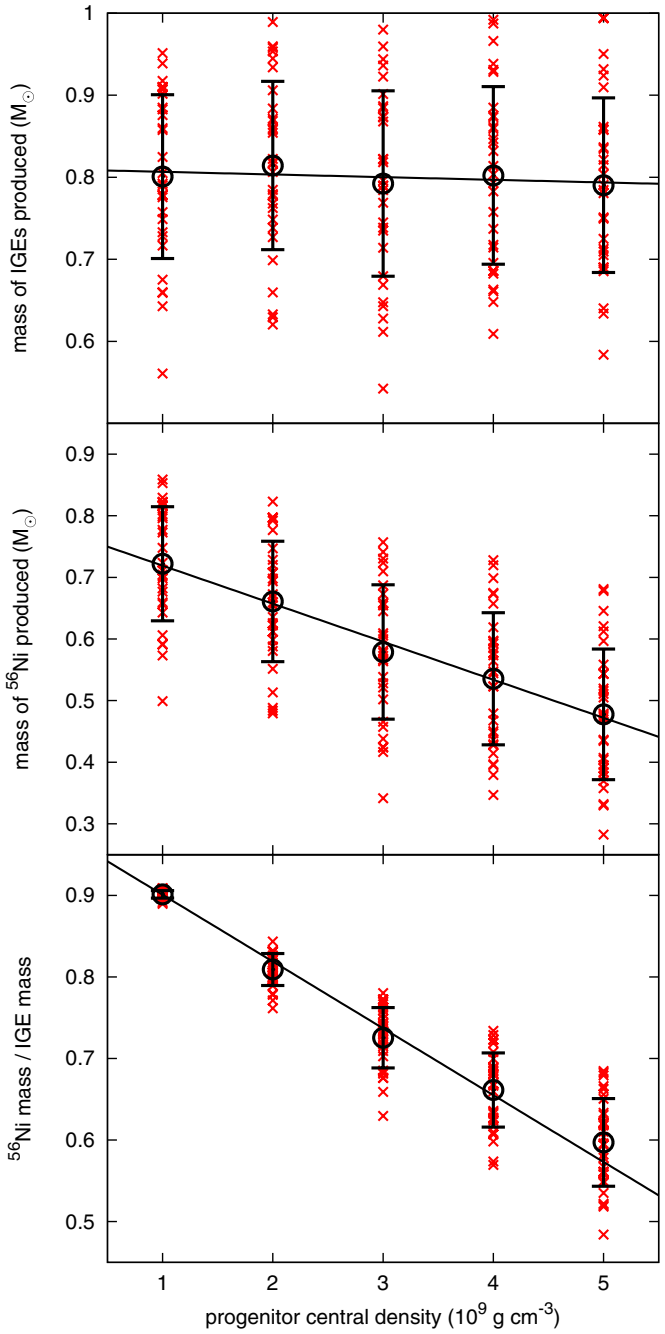

Figure 13. Final yields of our simulations after recalibration using Equations (B2) and (B3), the parameter values given in Table 5, and the time shifts given in Table 6. The black lines are the best-fit trend lines, with the averages and standard deviations marked by the circles and the vertical error bars. These plots are directly analogous to those shown in Figure 6.

(A color version of this figure is available in the online journal.)

our data do not, resulting in our data being overluminous relative to young SNe Ia. This study isolated the effects of central density and related that to age assuming a constant main-sequence mass, but there are other effects that may be correlated. Examples of such potentially correlated effects are main-sequence mass and its correlation with central density, metallicity of the progenitor, core ^{12}C fraction prior to ignition of the deflagration, sedimentation, and others. Inclusion of such effects may modify the results presented here and are the subjects of future work.

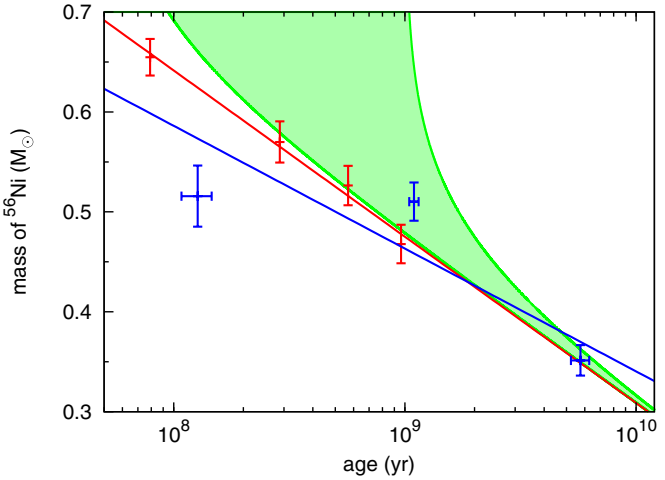

Figure 14. Plot of $M_{^{56}\mathrm{Ni}}$ vs. age comparing the scaled results of this study to the ^{56}Ni masses inferred from the observations of Neill et al. (2009). In red are the points from this study with no shift (i.e., $\tau_{\mathrm{MS}} = 0$ Gyr), along with the standard error of the mean and a best-fit trend line following the form of Equation (5). The green shaded region shows our best-fit line with $\tau_{\mathrm{MS}} = 0.05$–$1.0$ Gyr. In blue are the binned and averaged points from Figure 5 of Neill et al. (2009), along with their best-fit trend line.

(A color version of this figure is available in the online journal.)

5.3. Comparison to Other Theoretical Efforts

Recent theoretical work by other research groups also addresses the role of central density in the single-degenerate picture of SNe Ia. Fisher et al. (2010) note that in the gravitationally confined detonation (GCD) model (Plewa et al. 2004), a higher central density leads to increased energy release during the deflagration phase, which leads to increased expansion of the star and an increase in the production of intermediate-mass elements and the corresponding decrease in IGEs. These results are consistent with our findings concerning the choice of ρ_{DDT} influencing the production of IGEs discussed in Section 3.1.2. These results are also consistent with some of our realizations, but Fisher et al. (2010) do not consider the role of neutronization, preventing comparison to our principal result that the relative proportion of ^{56}Ni decreases with higher central density, producing a dimmer event.

Seitenzahl et al. (2011) performed a study of the DDT scenario with 3D simulations and a description of the flame energetics that accounts for neutronization. Seitenzahl et al. (2011) similarly find that the ^{56}Ni fraction of IGEs decreases in WD models with higher central densities, but they also find that the mass of IGEs increases at higher densities. The net effect is a roughly constant mass of ^{56}Ni synthesized during the explosion, implying that central density influences the brightness of an event only as a secondary parameter. Seitenzahl et al. (2011) comment on differences between their results and our earlier results (Krueger et al. 2010) and, likewise, we offer discussion here.

First, we note that our results are more similar than they might at first appear. Our trend of decreasing ^{56}Ni follows from the increased rate of neutronization at high densities of a roughly constant mass of IGEs synthesized during the explosion. In a sense, our trend is consistent with that of Seitenzahl et al. (2011). For a given mass of IGEs, the fraction that is ^{56}Ni is lower in WD models with a high central density. The difference between our results and those of Seitenzahl et al. (2011) follows from the increase in the mass of IGEs synthesized in their models. If

our explosions produced more IGEs for higher central density progenitors, then we may well see a roughly constant mass of ^{56}Ni. This observation should be readily apparent by considering Figure 6. If the flat slope of the IGE yield were instead rising enough, the decreasing slope of the ^{56}Ni yield would be instead rising. Accordingly, the key to the differences in our results is understanding the reason for the difference in the production of IGEs.

While there are many differences between the methodology of Seitenzahl et al. (2011) and ours, including (as they mention) differences in the flame model (level set versus ADR), differences in the energy release scheme, and structure of the computational mesh, perhaps the most substantive difference is the dimensionality of the simulations. Three-dimensional simulations meaningfully describe turbulent flow, which enables the use of TFI models. Turbulence in 2D simulations, however, has very different properties; particularly, it has an inverse cascade of energy from small to large scales (see chap. 10 of Davidson 2004, and references therein). Because of the large scope of this study, only 2D simulations were possible. As described above, our models use a flame speed that compensates for buoyancy effects to prevent the flame from being torn apart by Rayleigh–Taylor-induced turbulence. Because of the issue of turbulence in 2D simulations, we chose not to include models for unresolved turbulence and the TFI in our models for this study.

In their 3D simulations, Seitenzahl et al. (2011) similarly account for buoyancy effects, but also implement a method for accounting for turbulent energy on unresolved scales and the corresponding enhancement to the flame speed. Originally proposed by Niemeyer & Hillebrandt (1995) and developed in detail by Schmidt et al. (2006a, 2006b), the method consists of a dynamic measure of the local turbulent energy on sub-grid scales and sets the flame speed to $s = \sqrt{s_\ell^2 + C_t q^2}$, where q is a velocity that characterizes the sub-grid turbulence energy content and C_t is a constant taken to be 4/3. This addition should boost the burning rate during the deflagration phase, which will change the density profile of the star when the detonation occurs and thus change the final yield. It may be our omission of turbulence and TFI models that accounts for the systematic difference we see in the yield of IGEs as compared with those of Seitenzahl et al. (2011). While the difference in the treatment of the turbulent flame is a very important one, it is difficult to decouple this effect of the different dimensionality of the simulations performed. The dimensionality appears to influence the expansion rate, which may or may not be related to the turbulent flame model. Future 3D simulations with different turbulent flame models will be able to address these uncertainties.

Seitenzahl et al. (2011) also mention the choice of $\rho_{\rm DDT}$ as a possible source of the difference between their study and our earlier results. As they describe, Seitenzahl et al. (2011) use a dynamic measure that calculates the probability of a DDT based on the turbulent intensity, density, and fraction of fuel. As they note, this prescription is significantly different from just fixing $\rho_{\rm DDT}$ and results in fewer DDTs. Considering Table 1 of Seitenzahl et al. (2011), we can see that the density at which the DDT occurred appears to be a function of central density due to their DDT criteria: Other than their three models with only five DDT points, their effective DDT density increases with central density. A higher DDT density implies an earlier detonation, which means that the star has expanded less prior to the detonation, allowing the detonation to burn a larger fraction of the star. So it may be possible that the trend of increasing IGEs seen in Seitenzahl et al. (2011) comes from the change in their effective DDT density, instead of directly from the changing $\rho_{c,0}$. Regardless of whether this difference in methodology fully explains the difference in results, we can state that the differences in methodologies make direct comparison between the two results difficult.

Finally, the relatively small number of simulations performed by Seitenzahl et al. (2011) may not allow them to determine statistically meaningful trends. Unfortunately, the expense of 3D simulations make extensive studies difficult. The 12 simulations they performed are a remarkable achievement, but our results suggest that it is necessary to have a distribution of ignition conditions that reproduces the distribution of observed yields. Our statistical ensemble does this in 2D, but demonstrating such a distribution in 3D would require significant computational resources.

As Seitenzahl et al. (2011) mention, Meakin et al. (2009) explored the effect of varying the offset from the center of the initially burned region (what we call the "match head") in the GCD scenario. Their Figure 12 plots mass of NSE elements (which we have been referring to as IGEs), mass at $\rho > 10^7$ g cm^{-3}, and mass of ^{56}Ni as functions of central density *at the time of the detonation;* all of their models have the same central density at the ignition of the deflagration. We note that the GCD scenario is significantly different from the DDT scenario that we and Seitenzahl et al. (2011) investigated, with the principal difference arising in the expansion of the star during the deflagration phase of the evolution. In the GCD scenario, the star expands during the deflagration as the bubbles rise because the displaced mass softens the gravitational potential. The effect is that GCD models typically experience considerably less expansion than DDT models. Also, unlike central ignitions, there is very little material burned until the detonation occurs. A direct comparison, therefore, between the results of Meakin et al. (2009), with yields presented as functions of the central density at the ignition of the detonation, and our work, considering yields as a function of central density at the initial ignition of the deflagration, is at best uncertain, especially given that our results show that the effect of neutronization is the greatest during the deflagration phase as illustrated in Figure 7.

Röpke et al. (2006) performed a set of simulations of SNe Ia assuming the pure deflagration model. They found that as the central density of the progenitor is increased, the mass of ^{56}Ni produced also increases. Their discussion of why they produce more iron-group material also applies to our results. The yields during the deflagration and detonation phases were presented in Figure 7. We find the yield of IGEs increases with central density during the deflagration phase. We do not, however, find the same increase in ^{56}Ni mass due to increased neutronization. On this point our results disagree with the pure deflagration model as studied by Röpke et al. (2006). Bravo et al. (1990), however, studied the effects of neutronization and found that at higher central densities the yield of ^{56}Ni decreases, in agreement with our results.

Similarly to the Seitenzahl et al. (2011) work, Röpke et al. (2006) and Bravo et al. (1990) only performed a modest number of simulations. In light of our findings in Section 4.2, we note that it may be difficult to draw statistically significant results from a single realization. Röpke et al. (2006) and Bravo et al. (1990) both appear to use only a single morphology for each parameter set, which our results suggest could result in deriving an incorrect trend.

6. SUMMARY AND CONCLUSIONS

This paper builds on the results presented in Krueger et al. (2010), giving more detail of the study and extending the analysis. In that paper we showed that, in our 2D simulations, a higher central density of the progenitor star does not impact the production of IGEs, but leads to greater neutronization, resulting in the production of less ^{56}Ni. We also discussed the relation between the age of the progenitor and the central density (see, e.g., Lesaffre et al. 2006), and the relation between the brightness and the mass of ^{56}Ni produced. Thus, the statement that a higher density leads to less ^{56}Ni is equivalent to the statement that an older progenitor will produce a dimmer SN Ia. In this work, we expand on the discussion of Krueger et al. (2010) to give more detail of our models and to improve upon the age–brightness relation predicted by our simulations. In particular, we show that by adding a main-sequence lifetime to the cooling time our brightness–age relation is steeper, more closely matching the observed behavior of older SNe Ia.

In comparing with other theoretical work, we see that the variation of ^{56}Ni mass with progenitor central density is not a settled question. In this paper we further developed the idea that, due to the strong nonlinearities of the processes in SNe Ia, a statistical study of an ensemble of SN Ia simulations may be necessary to determine the true trends. For our simulations, we find that 15 realizations (morphologies of the initial flame surface) are sufficient to characterize the mean trends from our models.

We find that the inner region (out to an enclosed mass of 0.8–1.0 $M_\odot$) of the remnant is dominated by ^{56}Ni. However, the stable (non-^{56}Ni) IGEs tend to be in "clumps," instead of well mixed throughout this region. This may give rise to ^{56}Ni holes with little or no ^{56}Ni, depending on the line of sight through an SN Ia remnant. The outer region of the remnant will have more intermediate- and low-mass elements, as the burning becomes less efficient for lower densities. As the central density increases, the mean ^{56}Ni mass fraction in the inner region drops (roughly 0.8 for $\rho_{c,0} = 1 \times 10^9$ g cm^{-3} to roughly 0.6 for $\rho_{c,0} = 5 \times 10^9$ g cm^{-3}). However, the extent of this region (in enclosed-mass space) does not significantly change. Variations in the central density affect the sharpness of the edges of the stable IGE clumps: A higher central density leads to clumps of stable elements that are more sharply defined, as well as less mixing between the ^{56}Ni and the stable IGEs.

To better connect to observations, we discussed how to distinguish the relative ages of SNe Ia with the same brightness (in other words, the relative initial central densities of SNe Ia that produce the same mass of ^{56}Ni). We found that, in our models, the best measure of the central density is the mass of stable IGEs, where higher central density progenitors produce more stable IGEs due to their greater rate of neutronization during the subsonic deflagration phase.

We found that a higher central density leads to a shorter deflagration phase. Since the rate of neutronization is significantly boosted, the total neutronization is greater at a higher central density despite there being less time to neutronize. The time between the ignition of the first detonation and the cessation of burning is independent of central density.

As noted in Krueger et al. (2010) and described above, our choice for the DDT transition density led to an overproduction of ^{56}Ni. In Section 5.1, we provided a recalibration of this overall brightness normalization to extrapolate our results to an expected average brightness. Future work will be improved by a better choice of DDT density and we will report any quantitative changes to the trends reported here. Due to the fundamentally 3D nature of some of the phenomena in an SN Ia (such as the turbulent velocities), we plan to extend this work by performing 3D simulations. Because 3D simulations are much more computationally expensive than the corresponding 2D simulations, a study with 3D simulations will by necessity be constrained to a smaller number of simulations. The choices will be motivated by this work and seek to span the parameter space explored here.

This work was supported by the Department of Energy through grants DE-FG02-07ER41516, DE-FG02-08ER41570, and DE-FG02-08ER41565, and by NASA through grant NNX09AD19G. A.C.C. also acknowledges support from the Department of Energy under grant DE-FG02-87ER40317. A.P.J. is currently supported by a National Research Council Research Associateship. The authors gratefully acknowledge the generous assistance of Pierre Lesaffre, fruitful discussions with Mike Zingale, and the use of weak reaction tables developed by Ivo Seitenzahl. The authors also acknowledge the hospitality of the KITP, which is supported by NSF grant PHY05-51164, during the programs "Accretion and Explosion: the Astrophysics of Degenerate Stars" and "Stellar Death and Supernovae." The software used in this work was in part developed by the DOE-supported ASC/Alliances Center for Astrophysical Thermonuclear Flashes at the University of Chicago. We thank Nathan Hearn for making his QuickFlash analysis tools publicly available at http://quickflash.sourceforge.net. This research utilized resources at the New York Center for Computational Sciences at Stony Brook University/Brookhaven National Laboratory which is supported by the U.S. Department of Energy under Contract No. DE-AC02-98CH10886 and by the State of New York.

APPENDIX A

RANDOMIZED INITIAL CONDITIONS

The initial flame surfaces for each realization are determined by spherical harmonics. The formula used is

$$r = 150 \text{ km} + \sum_\ell A_\ell Y_\ell^m, \tag{A1}$$

where Y_ℓ^m are the spherical harmonics and the coefficients A_ℓ are given in Table 3. A reference implementation is available online at http://astronomy.ua.edu/townsley/code/. This suite of simulations used an initial seed value of 1,866,936,915.

APPENDIX B

RECALIBRATION OF ^{56}Ni YIELDS

As discussed above near the beginning of Section 4, on average our suite of simulations exhibited an overproduction of IGEs and ^{56}Ni. The yields of IGEs and ^{56}Ni are related to the expansion of the WD prior to the ignition of the detonation: As the star expands during the deflagration phase, the density decreases and, therefore, less fuel (C and O) remains at sufficiently high density to burn to IGEs during the detonation. Thus, the amount of expansion of the WD prior to the DDT principally determines the yield of IGEs and ^{56}Ni (Nomoto et al. 1984; Khokhlov 1991). The amount of expansion is

Table 3
Amplitudes of Spherical Harmonic Perturbations by Realization

Real. No.	Amplitude of Perturbation (km)				
	A_{12}	A_{13}	A_{14}	A_{15}	A_{16}
1	−50.88	−51.22	22.23	9.979	−56.23
2	−31.03	51.57	−43.21	−55.76	−30.22
3	−39.89	−28.06	31.48	6.848	−29.80
4	−48.89	−44.21	1.509	52.44	29.00
5	29.67	−74.12	−53.44	13.83	−51.24
6	−26.95	5.169	−45.79	−46.34	14.93
7	12.67	−19.76	−90.22	−2.312	−20.83
8	−10.23	1.206	−43.74	−25.57	10.26
9	30.25	69.91	−29.37	−74.17	−29.50
10	−15.76	−4.818	14.53	1.979	−15.23
11	−55.91	47.08	−15.86	−34.44	−43.00
12	1.021	−0.685	−33.13	−48.32	−22.22
13	−10.41	−32.27	5.236	27.06	−12.46
14	−73.60	−38.16	−22.76	41.81	25.76
15	−74.20	−3.179	−30.20	−36.56	−21.16
16	−86.84	16.28	19.75	14.43	4.924
17	12.87	44.39	−12.17	−34.34	−67.18
18	−13.88	−62.62	−35.93	−41.57	−81.32
19	−31.09	−49.91	2.953	57.76	−5.397
20	51.43	−44.30	−41.00	26.83	−42.83
21	−28.15	11.27	−37.43	85.20	−46.84
22	53.67	4.730	−52.71	−46.66	−65.99
23	−21.66	−12.31	53.21	14.14	−34.18
24	−16.25	−68.30	−43.63	111.6	−33.86
25	−56.50	−31.25	44.51	0.098	−40.66
26	−98.62	−31.80	−19.40	45.75	−3.815
27	−39.29	2.525	−32.95	27.10	−14.95
28	29.24	79.73	−30.80	−19.18	−96.98
29	−14.08	46.98	−89.82	−11.95	28.21
30	−24.91	33.12	−46.75	−10.40	−3.940

determined by DDT conditions (Jackson et al. 2010) along with the energy deposition history, which depends on initial conditions, dimensionality, and the burning model.

Given our models and the simulations we have performed, the most straightforward way to systematically correct the overproduction of IGEs is to modify the DDT conditions and repeat the simulations. The value of $\rho_{\rm DDT}$ should be determined by the physics of the DDT, but, as the physics of DDTs is incompletely understood and most likely could not be resolved in these simulations, we treat $\rho_{\rm DDT}$ as a parameter. The DDT transition is implemented by burning small regions ahead of rising plumes, when the tip of the plume reaches $\rho_{\rm DDT}$. As demonstrated in Jackson et al. (2010), lowering the value of $\rho_{\rm DDT}$ is tantamount to increasing $t_{\rm DDT}$ because the material that undergoes a DDT is at a higher radius and the time required for a rising bubble of burning material to reach that radius is longer. This longer $t_{\rm DDT}$ results in more expansion of the WD prior to detonation and, because the amount of material at higher density decreases, the detonation produces a lower yield of IGEs. In order to address the impact of $\rho_{\rm DDT}$ on our results, the ideal solution would be to repeat our simulations with $\rho_{\rm DDT}$ set to a lower value and therefore obtain a longer $t_{\rm DDT}$, more expansion, and more realistic yields. Using the data available from this study and the study of Jackson et al. (2010), we can estimate the results of performing a new suite of simulations using a different value of $\rho_{\rm DDT}$ and use these findings to inform future studies. We consider two issues here. First, we attempt to extrapolate to lower $\rho_{\rm DDT}$ based on the expansion characteristics of our models to confirm that for a *single value* of $\rho_{\rm DDT}$, the $M_{\rm IGE}$ appears to continue to be independent of $\rho_{c,0}$. Second, we use this justified assumption to extrapolate our yields based on a delay of the DDT transition.

Table 4
Fit Parameters for Equation (B1)

Parameter	Value
m_0	9.099×10^{-1}
γ_1	1.453×10^{-1}
γ_2	-2.429×10^{-2}
δ_1	-4.225×10^{-1}
δ_2	8.555×10^{-2}
b_0	8.358×10^{-3}
ε_1	-1.847×10^{-1}
ε_2	2.869×10^{-2}
ζ_1	6.231×10^{-1}
ζ_2	-1.196×10^{-1}

Note. These values assume that $\rho_{c,0}$ is in 10^9 g cm^{-3}, $\rho_{\rm DDT}$ is in 10^7 g cm^{-3}, and both masses are in $M_\odot$.

First, we consider how we expect $M_{\rm IGE}$ might change if a lower $\rho_{\rm DDT}$ were assumed. Townsley et al. (2009) demonstrate a correlation between $M_{\rm IGE}$ at $t_{\rm IGE}$ and the mass of all material with a density greater than 2×10^7 g cm^{-3} at time $t_{\rm DDT}$ (which we represent by $M^{\rm DDT}_{\rho_7>2}$). Therefore, we can choose a new value of $\rho_{\rm DDT}$ and use this correlation to estimate the final mass of IGEs in order to verify that changing $\rho_{\rm DDT}$ does not change the fact that the mass of IGEs is independent of $\rho_{c,0}$. In order to refine the relation between $M_{\rm IGE}$ and $M^{\rm DDT}_{\rho_7>2}$, we make use of data from this study and data from the study presented in Jackson et al. (2010), which varied $\rho_{\rm DDT}$. This will enable us to calibrate the relationship between $M_{\rm IGE}$ and $M^{\rm DDT}_{\rho_7>2}$ for differences in $\rho_{c,0}$ and $\rho_{\rm DDT}$. The relationship between $M_{\rm IGE}$ and $M^{\rm DDT}_{\rho_7>2}$ appears to be approximately linear, so we assume that $M_{\rm IGE} = m\ M^{\rm DDT}_{\rho_7>2} + b$. As can be seen in Figure 15, the relationship between $M^{\rm DDT}_{\rho_7>2}$ and $M_{\rm IGE}$ depends on $\rho_{c,0}$ and $\rho_{\rm DDT}$, so the slope and intercept are allowed to be functions of $\rho_{c,0}$ and $\rho_{\rm DDT}$. We test polynomials of varying degree and find that the best functions are quadratic in $\rho_{c,0}$ and $\rho_{\rm DDT}$ for both the slope and the intercept. The equations for this fitting are

$$M_{\rm IGE} = m(\rho_{c,0}, \rho_{\rm DDT})\ M^{\rm DDT}_{\rho_7>2} + b(\rho_{c,0}, \rho_{\rm DDT}), \tag{B1a}$$

$$m(\rho_{c,0}, \rho_{\rm DDT}) = m_0 + \gamma_1\rho_{c,0} + \gamma_2\rho^2_{c,0} + \delta_1\rho_{\rm DDT} + \delta_2\rho^2_{\rm DDT}, \tag{B1b}$$

$$b(\rho_{c,0}, \rho_{\rm DDT}) = b_0 + \varepsilon_1\rho_{c,0} + \varepsilon_2\rho^2_{c,0} + \zeta_1\rho_{\rm DDT} + \zeta_2\rho^2_{\rm DDT}. \tag{B1c}$$

Fitting this 10-parameter function to the data from this study and the study of Jackson et al. (2010) yields the parameters given in Table 4. As a check, we use this relation at the same $\rho_{\rm DDT}$ as was used in our simulations ($10^{7.1}$ g cm^{-3}) and compare the estimated values of $M_{\rm IGE}$ to the actual values. This is shown in Figure 16.

With this function, we can extract $M^{\rm DDT}_{\rho_7>2}$ assuming different values of $\rho_{\rm DDT}$. Based on the data available, we cannot choose a value of $\rho_{\rm DDT}$ lower than what used in this study, but we can test

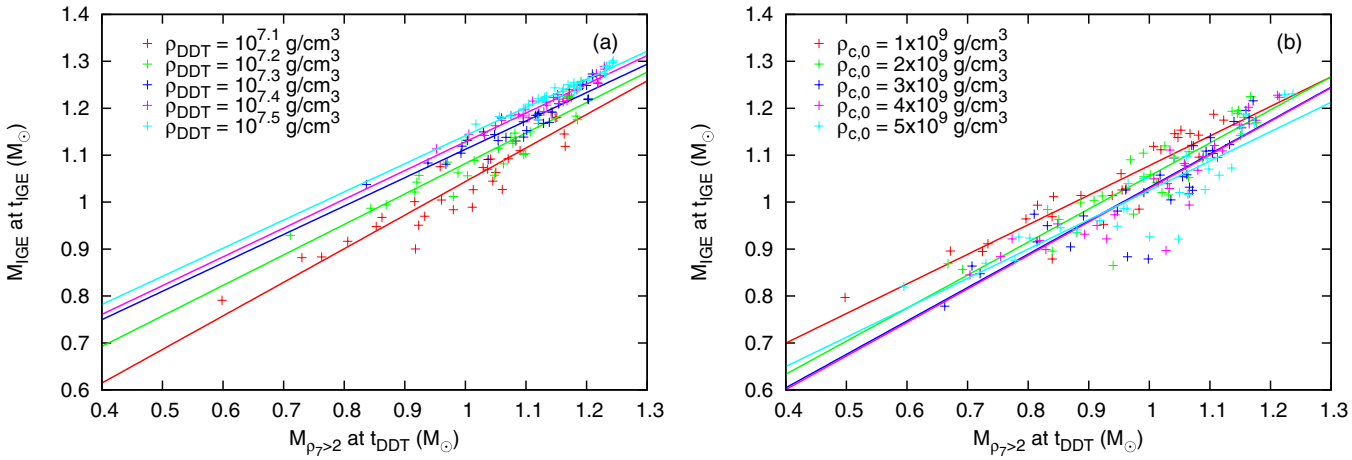

Figure 15. Relationship between $M_{\rho_{7>2}}^{\rm DDT}$ and $M_{\rm IGE}$, demonstrating the dependence of this relationship on $\rho_{c,0}$ and $\rho_{\rm DDT}$. The data in the left panel come from the study of Jackson et al. (2010), which varied $\rho_{\rm DDT}$ with a constant $\rho_{c,0}$; data points and trend lines are colored by $\rho_{\rm DDT}$. The data in the right panel come from this study; data points and trend lines are colored by $\rho_{c,0}$.

(A color version of this figure is available in the online journal.)

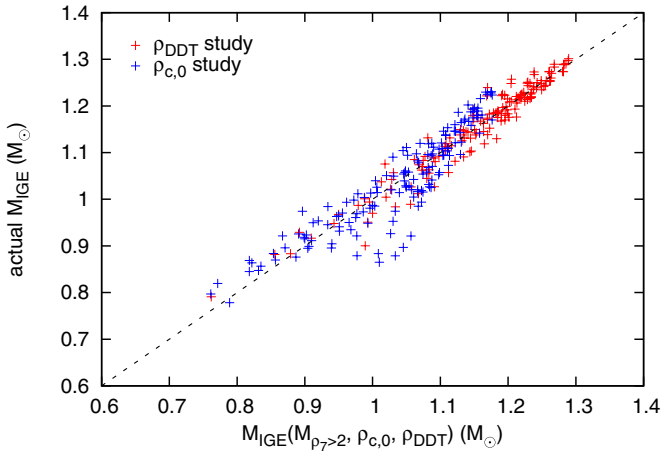

Figure 16. Demonstration of the results of Equation (B1), showing the comparison of the actual $M_{\rm IGE}$ data from simulations to the values of $M_{\rm IGE}$ estimated from this relation (assuming $\rho_{\rm DDT} = 10^{7.1}$ g cm^{-3}). Data points are colored by the study they were taken from: blue from this study and red from Jackson et al. (2010). The dotted line shows a perfect correspondence between the two measures of $M_{\rm IGE}$.

(A color version of this figure is available in the online journal.)

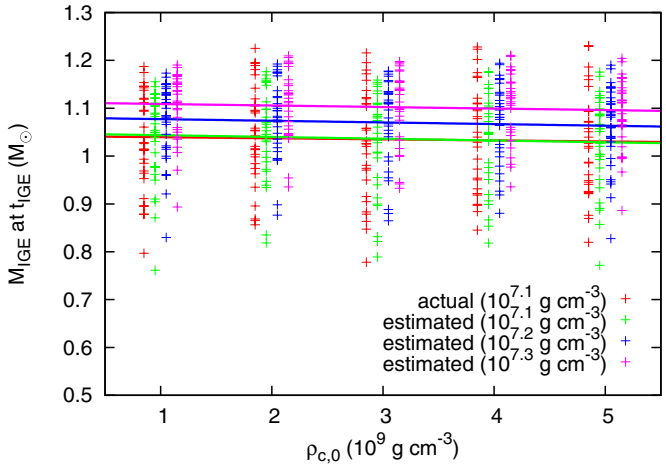

Figure 17. Demonstration of the results of Equation (B1), showing the trend of $M_{\rm IGE}$ with $\rho_{c,0}$, using data from this study. The values of $M_{\rm IGE}$ from the simulations are shown in red, with green, blue, and magenta showing the estimated $M_{\rm IGE}$ assuming $\rho_{\rm DDT} = 10^{7.1}$, $10^{7.2}$, and $10^{7.3}$ g cm^{-3}, respectively. The data points are slightly offset horizontally for clarity. This shows that $M_{\rm IGE}$ is independent of $\rho_{c,0}$ even if $\rho_{\rm DDT}$ varies. This figure also demonstrates that a lower value of $\rho_{\rm DDT}$ leads to a lower mean value of $M_{\rm IGE}$.

(A color version of this figure is available in the online journal.)

higher values of $\rho_{\rm DDT}$. Figure 17 shows that for three sample values of $\rho_{\rm DDT}$, $M_{\rm IGE}$ is still independent of $\rho_{c,0}$; formally, we say that $M_{\rm IGE}$ is independent of $\rho_{c,0}$ when the magnitude of the slope of the line relating these two quantities is less than the uncertainty in the slope. We therefore assume that, even for lower values of $\rho_{\rm DDT}$, $M_{\rm IGE}$ is independent of $\rho_{c,0}$. This allows us to apply a uniform shift in $M_{\rm IGE}$(constant for all simulations) to correct for the overproduction of IGEs. Observations tell us that the mass of IGEs should lie approximately in the range of 0.7–0.9 $M_\odot$ (see, e.g., Woosley et al. 2007), so we can choose to force our mean mass of IGEs to be in the center of this range (0.8 $M_\odot$).

Now that we have established a reasonable expectation that $M_{\rm IGE}$ will continue to be independent of $\rho_{c,0}$ even at other $\rho_{\rm DDT}$ values, we proceed to extrapolate our yields based around this premise. We can relate this change in $M_{\rm IGE}$ to a change in the mass of ^{56}Ni through adjustments to $t_{\rm DDT}$. The value of $t_{\rm DDT}$, which depends on $\rho_{\rm DDT}$, is not a free parameter that can be independently adjusted in our models; however, in order to correct the mass of ^{56}Ni we can treat $t_{\rm DDT}$ as a parameter. Figure 18 shows the masses of IGEs and ^{56}Ni plotted as functions of $t_{\rm DDT}$, where each point is a single simulation colored by $\rho_{c,0}$. Also shown is a trend line based on Equation (B2), explained below. Each of these quantities shows five separate trends, one for each value of $\rho_{c,0}$. Performing independent linear fits for each $\rho_{c,0}$ gives lines that appear to be correlated: The five lines intersect each other near $t_{\rm DDT} = 0$, and the slopes appear to be a function of $\rho_{c,0}$. Based on these correlations, we derived a new fit using the function

$$y(\rho_{c,0}, t_{\rm DDT}) = y_0 + s(\rho_{c,0})\, t_{\rm DDT}, \qquad \text{(B2)}$$

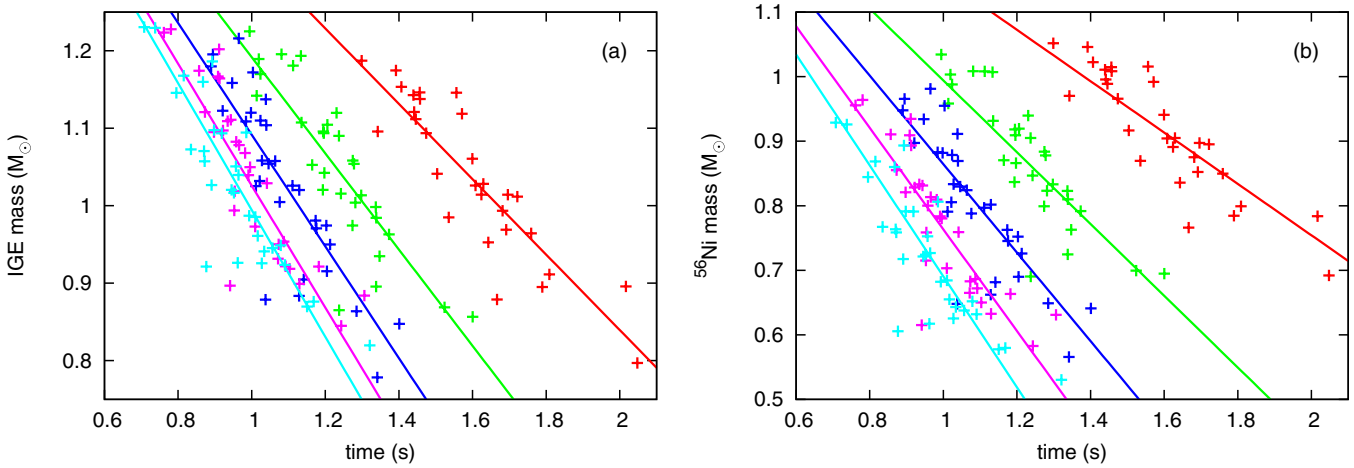

Figure 18. Yield of IGEs (left panel) and ^{56}Ni (right panel) as functions of $t_{\rm DDT}$ for the 149 simulations. Also shown are the best-fit trend lines in the form given by Equations (B2) and (B3). Lines and data points are colored by $\rho_{c,0}$: 1.0×10^9 g cm^{-3} (red), 2.0×10^9 g cm^{-3} (green), 3.0×10^9 g cm^{-3} (blue), 4.0×10^9 g cm^{-3} (magenta), and 5.0×10^9 g cm^{-3} (cyan).

(A color version of this figure is available in the online journal.)

Table 5
Fit Parameters for Equations (B2) and (B3)

Parameter	$M_{\rm IGE}$	$M_{^{56}\rm Ni}$
y_0	1.813	1.550
a	1.716×10^{-2}	1.422×10^{-2}
b	-1.859×10^{-1}	-2.007×10^{-1}
c	-3.180×10^{-1}	-2.114×10^{-1}

Note. These values assume that $t_{\rm DDT}$ is in seconds, $\rho_{c,0}$ is in 10^9 g cm^{-3}, and mass is in $M_\odot$.

Table 6
Time Shifts for the Recalibration of the ^{56}Ni and IGE Masses

$\rho_{c,0}$ (g cm^{-3})	$\Delta t_{\rm DDT}$ (s)
1×10^9	0.4850
2×10^9	0.3800
3×10^9	0.3273
4×10^9	0.2999
5×10^9	0.2884

where y is the mass of either IGEs or ^{56}Ni. We found that the best form for the slope $s(\rho_{c,0})$ is

$$s(\rho_{c,0}) = a\ \rho_{c,0}^2 + b\ \rho_{c,0} + c. \quad \text{(B3)}$$

Minimizing the χ^2_ν for this four-parameter function results in the parameter values shown in Table 5.

Given the shift in the mass of IGEs, we can then use the $M_{\rm IGE}(\rho_{c,0}, t_{\rm DDT})$ relation from Equations (B2) and (B3) to compute a corresponding change in $t_{\rm DDT}$. However, since the relation (in particular, the slope) depends on $\rho_{c,0}$, the time shift will also depend on $\rho_{c,0}$; i.e., we will have $\Delta t_{\rm DDT}(\rho_{c,0})$. The five values of $\Delta t_{\rm DDT}$ are given in Table 6. Using this density-dependent time shift and the $M_{^{56}\rm Ni}(\rho_{c,0}, t_{\rm DDT})$ relation, we can then derive a consistent adjustment to the mass of ^{56}Ni. This adjusted mass of ^{56}Ni is used in Section 5.1.

APPENDIX C
SIMULATION RESULTS

The structure and composition of the progenitor models are discussed in detail in Section 2.1, along with the creation of a statistical ensemble. The simulations and the code are discussed in Section 2. As we have stressed, the principal result from our simulations is a mass of ^{56}Ni. Our models reproduce the qualitative description given in Woosley et al. (2007) that produces an SN Ia light curve. The ideal solution for comparing our results to observed light would be for us to post-process our results with a radiation transfer method to actually calculate light curves. In the absence of that technology, we may infer observed properties of supernova events suggested by our results. We report some of those here, including stretch, the scaling of brightness with rapidity of decline that is reported in observational results (Howell et al. 2009; Jha et al. 2007). The tabulated data in Table 7 are as follows.

1. $\rho_{c,0}$: central density of pre-supernova WD (g cm^{-3}).
2. r: realization number.[9]
3. $t_{\rm DDT}$: time of the first DDT (s).
4. $M_{\rm IGE}(t_{\rm DDT})$: mass of IGEs synthesized by time $t_{\rm DDT}$ ($M_\odot$).
5. $M_{^{56}\rm Ni}(t_{\rm DDT})$: mass of ^{56}Ni synthesized by time $t_{\rm DDT}$ ($M_\odot$).
6. $t_{\rm IGE}$: time that the production of IGEs ceases (s).
7. $M_{\rm IGE}(t_{\rm IGE})$: mass of IGEs synthesized by time $t_{\rm IGE}$ ($M_\odot$).
8. $M_{^{56}\rm Ni}(t_{\rm IGE})$: mass of ^{56}Ni synthesized by time $t_{\rm IGE}$ ($M_\odot$).
9. $t^*_{\rm DDT}$: recalibrated[10] value of $t_{\rm DDT}$ (s).
10. $M^*_{\rm IGE}(t^*_{\rm IGE})$: recalibrated[10] value of $M_{\rm IGE}(t_{\rm IGE})$ ($M_\odot$).
11. $M^*_{^{56}\rm Ni}(t^*_{\rm IGE})$: recalibrated[10] value of $M_{^{56}\rm Ni}(t_{\rm IGE})$ ($M_\odot$).
12. s: recalibrated[10] value of stretch.[11]
13. $\tau_{\rm cool}$: cooling time[11] (yr).

The initial composition for the progenitor is shown in Table 2. The total mass of the star and the total mass of the initial convective, isentropic core are both shown for each progenitor in Table 1. Both of these tables are shown in Section 2.1.

[9] See Appendix A and Section 2 for more details.
[10] See Appendix B and Section 5.1 for details of the recalibration.
[11] See Section 5.2 for details of the derivation of s and $\tau_{\rm cool}$.

Table 7
Data Extracted from Simulations

$\rho_{c,0}$ (g cm^{-3})	r	$t_{\rm DDT}$ (s)	$M_{\rm IGE}(t_{\rm DDT})$ ($M_\odot$)	$M_{^{56}\rm Ni}(t_{\rm DDT})$ ($M_\odot$)	$t_{\rm IGE}$ (s)	$M_{\rm IGE}(t_{\rm IGE})$ ($M_\odot$)	$M_{^{56}\rm Ni}(t_{\rm IGE})$ ($M_\odot$)	$t^*_{\rm DDT}$ (s)	$M^*_{\rm IGE}(t^*_{\rm IGE})$ ($M_\odot$)	$M^*_{^{56}\rm Ni}(t^*_{\rm IGE})$ ($M_\odot$)	s	$\tau_{\rm cool}$ (yr)
1e+9	1	1.439	1.256e−1	7.744e−2	2.046	1.143e+0	1.011e+0	1.924	9.067e−1	8.177e−1	1.203	...[a]
1e+9	2	1.608	1.756e−1	1.210e−1	2.040	1.026e+0	9.042e−1	2.093	7.900e−1	7.112e−1	1.138	...[a]
1e+9	3	1.809	1.773e−1	1.229e−1	2.203	9.113e−1	7.991e−1	2.294	6.752e−1	6.061e−1	1.066	...[a]
1e+9	4	1.696	1.766e−1	1.256e−1	2.083	1.014e+0	8.972e−1	2.181	7.783e−1	7.042e−1	1.134	...[a]
1e+9	5	1.504	1.490e−1	9.677e−2	2.039	1.041e+0	9.166e−1	1.989	8.052e−1	7.237e−1	1.146	...[a]
1e+9	6	1.456	1.176e−1	7.158e−2	1.959	1.146e+0	1.015e+0	1.941	9.102e−1	8.217e−1	1.205	...[a]
1e+9	7	1.474	1.313e−1	8.181e−2	2.008	1.094e+0	9.659e−1	1.959	8.575e−1	7.729e−1	1.177	...[a]
1e+9	8	1.477	1.164e−1	6.855e−2	2.400	8.780e−1	7.687e−1	...[b]	...[b]	...[b]	...[b]	...[b]
1e+9	9	1.682	1.637e−1	1.110e−1	2.095	9.935e−1	8.751e−1	2.167	7.575e−1	6.822e−1	1.119	...[a]
1e+9	10	2.017	2.081e−1	1.495e−1	2.430	8.959e−1	7.837e−1	2.502	6.599e−1	5.907e−1	1.054	...[a]
1e+9	11	1.457	1.310e−1	8.431e−2	1.878	1.138e+0	1.008e+0	1.942	9.016e−1	8.155e−1	1.202	...[a]
1e+9	12	1.556	1.099e−1	6.654e−2	2.025	1.146e+0	1.016e+0	2.041	9.098e−1	8.227e−1	1.206	...[a]
1e+9	13	2.048	2.017e−1	1.429e−1	2.473	7.969e−1	6.920e−1	2.533	5.608e−1	4.990e−1	0.980	...[a]
1e+9	14	1.600	1.616e−1	1.135e−1	2.015	1.061e+0	9.410e−1	2.085	8.246e−1	7.480e−1	1.161	...[a]
1e+9	15	1.441	1.169e−1	7.452e−2	1.863	1.121e+0	9.955e−1	1.927	8.850e−1	8.026e−1	1.194	...[a]
1e+9	16	1.629	1.756e−1	1.198e−1	2.106	1.028e+0	9.049e−1	2.114	7.923e−1	7.120e−1	1.139	...[a]
1e+9	17	1.721	1.701e−1	1.204e−1	2.136	1.012e+0	8.951e−1	2.206	7.757e−1	7.021e−1	1.132	...[a]
1e+9	18	1.407	1.160e−1	7.173e−2	1.906	1.154e+0	1.022e+0	1.892	9.175e−1	8.295e−1	1.210	...[a]
1e+9	19	1.691	1.690e−1	1.157e−1	2.068	9.690e−1	8.524e−1	2.176	7.330e−1	6.594e−1	1.103	...[a]
1e+9	20	1.643	1.910e−1	1.341e−1	2.166	9.528e−1	8.358e−1	2.128	7.168e−1	6.428e−1	1.092	...[a]
1e+9	21	1.299	9.447e−2	5.357e−2	1.824	1.187e+0	1.052e+0	1.784	9.513e−1	8.589e−1	1.226	...[a]
1e+9	22	1.535	1.459e−1	9.739e−2	2.032	9.850e−1	8.697e−1	2.020	7.489e−1	6.767e−1	1.115	...[a]
1e+9	23	1.759	1.648e−1	1.131e−1	2.234	9.643e−1	8.498e−1	2.244	7.283e−1	6.568e−1	1.102	...[a]
1e+9	24	1.666	1.851e−1	1.265e−1	2.179	8.789e−1	7.662e−1	2.151	6.428e−1	5.732e−1	1.041	...[a]
1e+9	25	1.789	1.865e−1	1.315e−1	2.243	8.950e−1	7.846e−1	2.274	6.590e−1	5.916e−1	1.055	...[a]
1e+9	26	1.446	1.348e−1	9.107e−2	1.844	1.112e+0	9.889e−1	1.931	8.758e−1	7.959e−1	1.190	...[a]
1e+9	27	1.392	9.724e−2	6.110e−2	1.845	1.175e+0	1.046e+0	1.877	9.387e−1	8.530e−1	1.223	...[a]
1e+9	28	1.342	1.132e−1	7.015e−2	1.828	1.096e+0	9.702e−1	1.827	8.598e−1	7.772e−1	1.179	...[a]
1e+9	29	1.624	1.738e−1	1.169e−1	2.176	1.014e+0	8.911e−1	2.109	7.783e−1	6.981e−1	1.130	...[a]
1e+9	30	1.571	1.277e−1	8.167e−2	2.000	1.119e+0	9.920e−1	2.056	8.828e−1	7.990e−1	1.192	...[a]
2e+9	1	1.274	2.186e−1	1.056e−1	1.772	9.744e−1	7.991e−1	1.654	7.384e−1	5.879e−1	1.052	7.908e+7
2e+9	2	1.338	2.363e−1	1.183e−1	1.827	8.956e−1	7.246e−1	1.718	6.596e−1	5.133e−1	0.992	7.908e+7
2e+9	3	1.373	2.242e−1	1.122e−1	1.867	9.631e−1	7.917e−1	1.753	7.270e−1	5.804e−1	1.046	7.908e+7
2e+9	4	1.231	2.044e−1	9.844e−2	1.722	1.120e+0	9.398e−1	1.611	8.838e−1	7.285e−1	1.149	7.908e+7
2e+9	5	1.164	2.030e−1	9.237e−2	1.672	1.053e+0	8.705e−1	1.544	8.166e−1	6.592e−1	1.103	7.908e+7
2e+9	6	1.278	1.909e−1	8.627e−2	1.779	1.054e+0	8.780e−1	1.658	8.180e−1	6.668e−1	1.109	7.908e+7
2e+9	7	1.237	1.942e−1	8.247e−2	1.628	1.090e+0	9.049e−1	1.617	8.541e−1	6.936e−1	1.127	7.908e+7
2e+9	8	1.196	1.727e−1	6.563e−2	1.789	1.094e+0	9.092e−1	1.576	8.577e−1	6.979e−1	1.129	7.908e+7
2e+9	9	1.281	2.196e−1	1.018e−1	1.742	1.004e+0	8.231e−1	1.661	7.678e−1	6.118e−1	1.070	7.908e+7
2e+9	10	1.600	2.540e−1	1.408e−1	2.141	8.565e−1	6.948e−1	1.980	6.205e−1	4.835e−1	0.967	7.908e+7
2e+9	11	1.195	1.883e−1	8.399e−2	1.598	1.096e+0	9.183e−1	1.575	8.598e−1	7.070e−1	1.135	7.908e+7
2e+9	12	1.134	1.356e−1	4.169e−2	1.604	1.194e+0	1.007e+0	1.514	9.575e−1	7.957e−1	1.190	7.908e+7
2e+9	13	1.524	2.363e−1	1.168e−1	1.957	8.689e−1	6.994e−1	1.904	6.328e−1	4.882e−1	0.971	7.908e+7
2e+9	14	1.242	2.062e−1	1.029e−1	1.727	1.016e+0	8.468e−1	1.622	7.795e−1	6.356e−1	1.087	7.908e+7
2e+9	15	1.024	1.429e−1	5.202e−2	1.569	1.170e+0	9.880e−1	1.404	9.340e−1	7.768e−1	1.179	7.908e+7
2e+9	16	1.347	2.412e−1	1.257e−1	1.816	9.349e−1	7.629e−1	1.727	6.988e−1	5.516e−1	1.024	7.908e+7
2e+9	17	1.275	2.046e−1	9.945e−2	1.704	1.058e+0	8.838e−1	1.655	8.223e−1	6.726e−1	1.112	7.908e+7
2e+9	18	1.019	1.490e−1	5.379e−2	1.586	1.189e+0	1.003e+0	1.399	9.533e−1	7.921e−1	1.188	7.908e+7
2e+9	19	1.206	1.913e−1	8.005e−2	1.619	1.105e+0	9.195e−1	1.586	8.685e−1	7.083e−1	1.136	7.908e+7
2e+9	20	1.298	2.323e−1	1.153e−1	1.716	1.013e+0	8.333e−1	1.678	7.774e−1	6.220e−1	1.077	7.908e+7
2e+9	21	0.994	1.383e−1	4.546e−2	1.503	1.225e+0	1.034e+0	1.374	9.892e−1	8.231e−1	1.206	7.908e+7
2e+9	22	1.197	1.861e−1	8.048e−2	1.792	1.043e+0	8.660e−1	1.577	8.065e−1	6.548e−1	1.100	7.908e+7
2e+9	23	1.337	2.027e−1	9.030e−2	1.780	9.984e−1	8.230e−1	1.717	7.624e−1	6.117e−1	1.070	7.908e+7
2e+9	24	1.237	2.299e−1	1.069e−1	1.870	8.652e−1	6.905e−1	1.617	6.291e−1	4.792e−1	0.963	7.908e+7
2e+9	25	1.338	2.190e−1	1.059e−1	1.736	9.844e−1	8.099e−1	1.718	7.484e−1	5.986e−1	1.060	7.908e+7
2e+9	26	1.135	1.792e−1	7.881e−2	1.557	1.107e+0	9.315e−1	1.515	8.714e−1	7.202e−1	1.144	7.908e+7
2e+9	27	1.112	1.329e−1	4.918e−2	1.539	1.181e+0	1.008e+0	1.492	9.448e−1	7.970e−1	1.191	7.908e+7
2e+9	28	1.014	1.529e−1	5.527e−2	1.451	1.142e+0	9.583e−1	1.394	9.059e−1	7.471e−1	1.161	7.908e+7
2e+9	29	1.193	2.064e−1	8.958e−2	1.766	1.021e+0	8.368e−1	1.573	7.845e−1	6.255e−1	1.080	7.908e+7
2e+9	30	1.081	1.509e−1	5.572e−2	1.529	1.196e+0	1.008e+0	1.461	9.596e−1	7.971e−1	1.191	7.908e+7
3e+9	1	1.111	2.392e−1	8.266e−2	1.533	1.026e+0	7.969e−1	1.438	7.899e−1	5.726e−1	1.040	2.879e+8
3e+9	2	1.064	2.459e−1	8.436e−2	1.503	1.058e+0	8.240e−1	1.391	8.217e−1	5.997e−1	1.061	2.879e+8
3e+9	3	1.285	2.507e−1	8.898e−2	1.723	8.638e−1	6.488e−1	1.612	6.278e−1	4.244e−1	0.911	2.879e+8
3e+9	4	1.174	2.375e−1	8.843e−2	1.751	9.808e−1	7.627e−1	1.501	7.448e−1	5.383e−1	1.013	2.879e+8
3e+9	5	1.022	2.249e−1	7.251e−2	1.556	1.032e+0	8.054e−1	1.349	7.958e−1	5.810e−1	1.047	2.879e+8

Table 7
(Continued)

$\rho_{c,0}$ (g cm^{-3})	r	$t_{\rm DDT}$ (s)	$M_{\rm IGE}(t_{\rm DDT})$ ($M_\odot$)	$M_{^{56}{\rm Ni}}(t_{\rm DDT})$ ($M_\odot$)	$t_{\rm IGE}$ (s)	$M_{\rm IGE}(t_{\rm IGE})$ ($M_\odot$)	$M_{^{56}{\rm Ni}}(t_{\rm IGE})$ ($M_\odot$)	$t^*_{\rm DDT}$ (s)	$M^*_{\rm IGE}(t^*_{\rm IGE})$ ($M_\odot$)	$M^*_{^{56}{\rm Ni}}(t^*_{\rm IGE})$ ($M_\odot$)	s	$\tau_{\rm cool}$ (yr)
3e+9	6	1.024	1.950e−1	4.817e−2	1.531	1.110e+0	8.787e−1	1.351	8.739e−1	6.544e−1	1.100	2.879e+8
3e+9	7	0.998	2.130e−1	5.642e−2	1.414	1.120e+0	8.818e−1	1.325	8.841e−1	6.575e−1	1.102	2.879e+8
3e+9	8	1.039	2.016e−1	5.049e−2	1.538	1.104e+0	8.693e−1	1.367	8.679e−1	6.449e−1	1.093	2.879e+8
3e+9	9	1.141	2.510e−1	8.595e−2	1.652	9.048e−1	6.815e−1	1.469	6.687e−1	4.571e−1	0.943	2.879e+8
3e+9	10	1.401	2.650e−1	1.099e−1	1.881	8.474e−1	6.409e−1	1.728	6.114e−1	4.165e−1	0.903	2.879e+8
3e+9	11	1.046	2.204e−1	6.880e−2	1.484	1.054e+0	8.297e−1	1.373	8.182e−1	6.054e−1	1.065	2.879e+8
3e+9	12	0.965	1.622e−1	3.069e−2	1.478	1.216e+0	9.813e−1	1.292	9.799e−1	7.569e−1	1.167	2.879e+8
3e+9	13	1.341	2.612e−1	9.459e−2	1.777	7.783e−1	5.657e−1	1.669	5.423e−1	3.414e−1	0.821	2.879e+8
3e+9	14	1.076	2.186e−1	7.401e−2	1.578	1.005e+0	7.881e−1	1.403	7.688e−1	5.637e−1	1.033	2.879e+8
3e+9	15	0.947	1.748e−1	4.569e−2	1.413	1.159e+0	9.341e−1	1.274	9.226e−1	7.097e−1	1.137	2.879e+8
3e+9	16	1.129	2.631e−1	9.851e−2	1.664	8.836e−1	6.622e−1	1.456	6.475e−1	4.378e−1	0.924	2.879e+8
3e+9	17	1.129	2.272e−1	7.756e−2	1.589	1.020e+0	8.019e−1	1.456	7.843e−1	5.775e−1	1.044	2.879e+8
3e+9	18	0.890	1.738e−1	4.342e−2	1.426	1.180e+0	9.478e−1	1.217	9.438e−1	7.235e−1	1.146	2.879e+8
3e+9	19	1.204	2.529e−1	8.665e−2	1.639	9.155e−1	6.899e−1	1.531	6.794e−1	4.655e−1	0.950	2.879e+8
3e+9	20	1.176	2.544e−1	9.120e−2	1.608	9.708e−1	7.453e−1	1.503	7.347e−1	5.210e−1	0.999	2.879e+8
3e+9	21	0.895	1.713e−1	4.005e−2	1.403	1.195e+0	9.655e−1	1.222	9.594e−1	7.411e−1	1.157	2.879e+8
3e+9	22	1.028	2.095e−1	6.057e−2	1.509	1.058e+0	8.335e−1	1.355	8.223e−1	6.092e−1	1.068	2.879e+8
3e+9	23	1.213	2.392e−1	7.568e−2	1.626	9.500e−1	7.260e−1	1.540	7.139e−1	5.017e−1	0.982	2.879e+8
3e+9	24	1.038	2.525e−1	8.053e−2	1.647	8.788e−1	6.479e−1	1.365	6.428e−1	4.236e−1	0.910	2.879e+8
3e+9	25	1.203	2.463e−1	9.050e−2	1.629	9.745e−1	7.522e−1	1.530	7.384e−1	5.278e−1	1.004	2.879e+8
3e+9	26	0.984	2.020e−1	5.757e−2	1.385	1.109e+0	8.828e−1	1.312	8.728e−1	6.584e−1	1.103	2.879e+8
3e+9	27	1.003	1.638e−1	3.844e−2	1.433	1.172e+0	9.547e−1	1.331	9.360e−1	7.304e−1	1.150	2.879e+8
3e+9	28	0.921	1.909e−1	5.010e−2	1.375	1.123e+0	8.973e−1	1.249	8.866e−1	6.729e−1	1.113	2.879e+8
3e+9	29	1.011	2.293e−1	6.818e−2	1.490	1.025e+0	7.908e−1	1.339	7.894e−1	5.665e−1	1.036	2.879e+8
3e+9	30	1.038	1.857e−1	4.406e−2	1.473	1.137e+0	9.113e−1	1.366	9.013e−1	6.869e−1	1.122	2.879e+8
4e+9	1	0.996	2.532e−1	6.652e−2	1.449	1.050e+0	7.802e−1	1.295	8.138e−1	5.443e−1	1.018	5.682e+8
4e+9	2	0.958	2.501e−1	5.462e−2	1.376	1.083e+0	8.002e−1	1.258	8.465e−1	5.642e−1	1.034	5.682e+8
4e+9	3	1.182	2.528e−1	5.884e−2	1.581	9.215e−1	6.633e−1	1.482	6.855e−1	4.274e−1	0.914	5.682e+8
4e+9	4	1.092	2.416e−1	6.524e−2	1.683	9.218e−1	6.719e−1	1.392	6.857e−1	4.359e−1	0.922	5.682e+8
4e+9	5	0.898	2.296e−1	4.362e−2	1.344	1.095e+0	8.208e−1	1.198	8.589e−1	5.848e−1	1.050	5.682e+8
4e+9	6	0.935	2.141e−1	3.618e−2	1.436	1.109e+0	8.331e−1	1.235	8.732e−1	5.972e−1	1.059	5.682e+8
4e+9	7	0.943	2.383e−1	4.479e−2	1.390	1.111e+0	8.314e−1	1.243	8.749e−1	5.954e−1	1.058	5.682e+8
4e+9	8	1.041	2.287e−1	3.968e−2	1.524	1.029e+0	7.590e−1	1.341	7.930e−1	5.231e−1	1.001	5.682e+8
4e+9	9	1.009	2.551e−1	5.758e−2	1.513	9.731e−1	7.033e−1	1.309	7.370e−1	4.673e−1	0.952	5.682e+8
4e+9	10	1.306	2.604e−1	6.975e−2	1.739	8.840e−1	6.309e−1	1.606	6.479e−1	3.950e−1	0.881	5.682e+8
4e+9	11	0.966	2.429e−1	5.893e−2	1.385	1.078e+0	8.134e−1	1.266	8.423e−1	5.775e−1	1.044	5.682e+8
4e+9	12	0.911	1.863e−1	2.445e−2	1.411	1.202e+0	9.346e−1	1.211	9.661e−1	6.986e−1	1.130	5.682e+8
4e+9	13	1.243	2.776e−1	7.328e−2	1.693	8.450e−1	5.828e−1	1.543	6.090e−1	3.468e−1	0.828	5.682e+8
4e+9	14	0.991	2.307e−1	5.550e−2	1.432	1.040e+0	7.836e−1	1.291	8.035e−1	5.477e−1	1.021	5.682e+8
4e+9	15	0.857	1.973e−1	3.404e−2	1.295	1.174e+0	9.107e−1	1.157	9.383e−1	6.747e−1	1.114	5.682e+8
4e+9	16	1.072	2.842e−1	8.135e−2	1.520	9.316e−1	6.651e−1	1.372	6.956e−1	4.291e−1	0.916	5.682e+8
4e+9	17	0.982	2.230e−1	5.106e−2	1.475	1.068e+0	8.094e−1	1.282	8.320e−1	5.735e−1	1.041	5.682e+8
4e+9	18	0.761	1.836e−1	3.043e−2	1.272	1.224e+0	9.556e−1	1.061	9.875e−1	7.196e−1	1.143	5.682e+8
4e+9	19	1.103	2.649e−1	6.228e−2	1.518	9.185e−1	6.502e−1	1.403	6.824e−1	4.142e−1	0.901	5.682e+8
4e+9	20	1.087	2.577e−1	6.216e−2	1.549	9.537e−1	6.863e−1	1.387	7.177e−1	4.504e−1	0.936	5.682e+8
4e+9	21	0.780	1.877e−1	2.909e−2	1.286	1.228e+0	9.640e−1	1.080	9.919e−1	7.281e−1	1.149	5.682e+8
4e+9	22	0.954	2.283e−1	4.964e−2	1.456	1.019e+0	7.587e−1	1.254	7.827e−1	5.227e−1	1.000	5.682e+8
4e+9	23	1.130	2.532e−1	5.409e−2	1.637	8.991e−1	6.326e−1	1.430	6.631e−1	3.966e−1	0.883	5.682e+8
4e+9	24	0.941	2.751e−1	5.869e−2	1.506	8.969e−1	6.151e−1	1.241	6.608e−1	3.791e−1	0.864	5.682e+8
4e+9	25	1.073	2.644e−1	6.909e−2	1.538	9.503e−1	6.829e−1	1.373	7.142e−1	4.470e−1	0.933	5.682e+8
4e+9	26	0.922	2.217e−1	4.436e−2	1.397	1.097e+0	8.284e−1	1.222	8.612e−1	5.924e−1	1.055	5.682e+8
4e+9	27	0.909	1.905e−1	3.106e−2	1.348	1.167e+0	9.091e−1	1.209	9.308e−1	6.731e−1	1.113	5.682e+8
4e+9	28	0.873	2.169e−1	4.070e−2	1.321	1.121e+0	8.550e−1	1.173	8.848e−1	6.191e−1	1.075	5.682e+8
4e+9	29	0.953	2.442e−1	4.582e−2	1.522	9.938e−1	7.150e−1	1.253	7.577e−1	4.790e−1	0.963	5.682e+8
4e+9	30	0.912	1.922e−1	2.870e−2	1.418	1.164e+0	8.932e−1	1.212	9.284e−1	6.573e−1	1.102	5.682e+8
5e+9	1	0.993	2.659e−1	5.307e−2	1.441	9.871e−1	6.823e−1	1.282	7.510e−1	4.344e−1	0.921	9.625e+8
5e+9	2	0.964	2.683e−1	4.278e−2	1.357	1.040e+0	7.268e−1	1.252	8.037e−1	4.789e−1	0.962	9.625e+8
5e+9	3	1.151	2.732e−1	4.979e−2	1.593	8.698e−1	5.775e−1	1.439	6.338e−1	3.296e−1	0.807	9.625e+8
5e+9	4	1.010	2.522e−1	4.409e−2	1.589	9.855e−1	6.843e−1	1.298	7.495e−1	4.364e−1	0.923	9.625e+8
5e+9	5	0.835	2.397e−1	3.034e−2	1.303	1.073e+0	7.673e−1	1.123	8.366e−1	5.195e−1	0.998	9.625e+8
5e+9	6	0.919	2.352e−1	3.124e−2	1.425	1.094e+0	7.911e−1	1.207	8.575e−1	5.432e−1	1.017	9.625e+8
5e+9	7	0.871	2.459e−1	3.091e−2	1.368	1.071e+0	7.635e−1	1.159	8.346e−1	5.157e−1	0.994	9.625e+8
5e+9	8	1.079	2.583e−1	4.057e−2	1.553	9.488e−1	6.520e−1	1.367	7.127e−1	4.042e−1	0.891	9.625e+8
5e+9	9	1.028	2.723e−1	3.992e−2	1.438	9.257e−1	6.253e−1	1.316	6.897e−1	3.775e−1	0.862	9.625e+8
5e+9	10	1.321	2.654e−1	3.999e−2	1.744	8.197e−1	5.304e−1	1.609	5.836e−1	2.825e−1	0.746	9.625e+8

Table 7
(Continued)

$\rho_{c,0}$ (g cm^{-3})	r	$t_{\rm DDT}$ (s)	$M_{\rm IGE}(t_{\rm DDT})$ ($M_\odot$)	$M_{^{56}{\rm Ni}}(t_{\rm DDT})$ ($M_\odot$)	$t_{\rm IGE}$ (s)	$M_{\rm IGE}(t_{\rm IGE})$ ($M_\odot$)	$M_{^{56}{\rm Ni}}(t_{\rm IGE})$ ($M_\odot$)	$t^*_{\rm DDT}$ (s)	$M^*_{\rm IGE}(t^*_{\rm IGE})$ ($M_\odot$)	$M^*_{^{56}{\rm Ni}}(t^*_{\rm IGE})$ ($M_\odot$)	s	$\tau_{\rm cool}$ (yr)
5e+9	11	0.945	2.598e−1	4.614e−2	1.369	1.020e+0	7.213e−1	1.234	7.844e−1	4.735e−1	0.958	9.625e+8
5e+9	12	0.893	2.114e−1	2.626e−2	1.402	1.186e+0	8.934e−1	1.181	9.502e−1	6.455e−1	1.094	9.625e+8
5e+9	13	1.168	2.718e−1	4.903e−2	1.658	8.762e−1	5.797e−1	1.457	6.401e−1	3.318e−1	0.810	9.625e+8
5e+9	14	0.957	2.477e−1	4.220e−2	1.356	1.051e+0	7.527e−1	1.246	8.148e−1	5.048e−1	0.985	9.625e+8
5e+9	15	0.816	2.211e−1	3.014e−2	1.230	1.168e+0	8.686e−1	1.104	9.317e−1	6.207e−1	1.076	9.625e+8
5e+9	16	0.962	2.841e−1	5.486e−2	1.476	9.264e−1	6.173e−1	1.250	6.903e−1	3.694e−1	0.854	9.625e+8
5e+9	17	0.952	2.412e−1	3.602e−2	1.394	1.017e+0	7.242e−1	1.240	7.806e−1	4.764e−1	0.960	9.625e+8
5e+9	18	0.708	1.996e−1	2.283e−2	1.240	1.231e+0	9.288e−1	0.996	9.945e−1	6.809e−1	1.118	9.625e+8
5e+9	19	1.056	2.749e−1	4.684e−2	1.514	9.454e−1	6.377e−1	1.345	7.093e−1	3.898e−1	0.876	9.625e+8
5e+9	20	1.017	2.628e−1	3.967e−2	1.450	9.610e−1	6.549e−1	1.305	7.250e−1	4.070e−1	0.894	9.625e+8
5e+9	21	0.738	2.054e−1	2.201e−2	1.248	1.230e+0	9.259e−1	1.026	9.936e−1	6.781e−1	1.116	9.625e+8
5e+9	22	0.872	2.439e−1	4.205e−2	1.420	1.057e+0	7.587e−1	1.160	8.213e−1	5.108e−1	0.990	9.625e+8
5e+9	23	1.090	2.600e−1	3.872e−2	1.487	9.235e−1	6.318e−1	1.379	6.874e−1	3.839e−1	0.869	9.625e+8
5e+9	24	0.877	2.843e−1	4.293e−2	1.417	9.215e−1	6.055e−1	1.165	6.854e−1	3.577e−1	0.840	9.625e+8
5e+9	25	1.034	2.672e−1	4.927e−2	1.469	9.410e−1	6.431e−1	1.323	7.050e−1	3.952e−1	0.881	9.625e+8
5e+9	26	0.898	2.510e−1	4.255e−2	1.344	1.098e+0	7.913e−1	1.186	8.615e−1	5.435e−1	1.017	9.625e+8
5e+9	27	0.985	2.265e−1	3.279e−2	1.413	1.094e+0	8.063e−1	1.274	8.583e−1	5.584e−1	1.029	9.625e+8
5e+9	28	0.795	2.264e−1	2.744e−2	1.272	1.146e+0	8.445e−1	1.084	9.096e−1	5.966e−1	1.059	9.625e+8
5e+9	29	0.891	2.486e−1	3.129e−2	1.406	1.027e+0	7.174e−1	1.180	7.907e−1	4.695e−1	0.954	9.625e+8
5e+9	30	0.868	2.162e−1	2.560e−2	1.343	1.160e+0	8.600e−1	1.156	9.239e−1	6.122e−1	1.070	9.625e+8

Notes.
[a] As discussed in Section 5.2, the results of Lesaffre et al. (2006) do not allow us to generate cooling times for results with $\rho_{c,0} = 1.0 \times 10^9$ g cm^{-3}.
[b] As discussed in Section 3.1.2, the results of $\rho_{c,0} = 1.0 \times 10^9$ g cm^{-3}, realization 8, were excluded from the analysis.

REFERENCES

Albrecht, A., Bernstein, G., Cahn, R., et al. 2006, arXiv:astro-ph/0609591
Arnett, W. D. 1982, ApJ, 253, 785
Aspden, A. J., Bell, J. B., Day, M. S., Woosley, S. E., & Zingale, M. 2008, ApJ, 689, 1173
Aspden, A. J., Bell, J. B., & Woosley, S. E. 2010, ApJ, 710, 1654
Blinnikov, S. I., & Khokhlov, A. M. 1986, Sov. Astron. Lett., 12, 131
Bloom, J. S., Kasen, D., Shen, K. J., et al. 2012, ApJ, 744, L17
Branch, D., Livio, M., Yungelson, L. R., Boffi, F. R., & Baron, E. 1995, PASP, 107, 1019
Brandt, T. D., Tojeiro, R., Aubourg, É., et al. 2010, AJ, 140, 804
Bravo, E., & García-Senz, D. 2008, A&A, 478, 843
Bravo, E., Isern, J., Canal, R., & Labay, J. 1990, Ap&SS, 169, 19
Calder, A. C., Fryxell, B., Plewa, T., et al. 2002, ApJS, 143, 201
Calder, A. C., Townsley, D. M., Seitenzahl, I. R., et al. 2007, ApJ, 656, 313
Chamulak, D. A., Brown, E. F., Timmes, F. X., & Dupczak, K. 2008, ApJ, 677, 160
Colgate, S. A., & McKee, C. 1969, ApJ, 157, 623
Conley, A., Guy, J., Sullivan, M., et al. 2011, ApJS, 192, 1
Davidson, P. A. 2004, Turbulence (Oxford: Oxford Univ. Press)
Domínguez, I., Höflich, P., & Straniero, O. 2001, ApJ, 557, 279
Filippenko, A. V. 1997, ARA&A, 35, 309
Fisher, R., Falta, D., Jordan, G., & Lamb, D. 2010, in Gravitation and Astrophysics, ed. J. Luo, Z.-B. Zhou, H.-C. Yeh, & J.-P. Hsu (Singapore: World Scientific), 335
Fryxell, B., Olson, K., Ricker, P., et al. 2000, ApJS, 131, 273
Fuller, G. M., Fowler, W. A., & Newman, M. J. 1985, ApJ, 293, 1
Gallagher, J. S., Garnavich, P. M., Caldwell, N., et al. 2008, ApJ, 685, 752
Golombek, I., & Niemeyer, J. C. 2005, A&A, 438, 611
Hansen, C. J., Kawaler, S. D., & Trimble, V. (ed.) 2004, Stellar Interiors: Physical Principles, Structure, and Evolution (New York: Springer)
Hillebrandt, W., & Niemeyer, J. C. 2000, ARA&A, 38, 191
Höflich, P., Wheeler, J. C., & Thielemann, F. K. 1998, ApJ, 495, 617
Höflich, P., & Khokhlov, A. 1996, ApJ, 457, 500
Höflich, P., Khokhlov, A. M., & Wheeler, J. C. 1995, ApJ, 444, 831
Höflich, P., Krisciunas, K., Khokhlov, A. M., et al. 2010, ApJ, 710, 444
Howell, D. A., Sullivan, M., Brown, E. F., et al. 2009, ApJ, 691, 661
Jackson, A. P., Calder, A. C., Townsley, D. M., et al. 2010, ApJ, 720, 99
Jacoby, G. H., Branch, D., Ciardullo, R., et al. 1992, PASP, 104, 599
Jha, S., Riess, A. G., & Kirshner, R. P. 2007, ApJ, 659, 122
Khokhlov, A. M. 1989, MNRAS, 239, 785
Khokhlov, A. M. 1991, A&A, 245, 114
Khokhlov, A. M. 1995, ApJ, 449, 695
Khokhlov, A. M. 2000, arXiv:astro-ph/0008463
Khokhlov, A. M., Oran, E. S., & Wheeler, J. C. 1997, ApJ, 478, 678
Kirshner, R. P. 2010, in Foundations of Supernova Cosmology, ed. P. Ruiz-Lapuente (New York: Cambridge Univ. Press), 151
Krueger, B. K., Jackson, A. P., Townsley, D. M., et al. 2010, ApJ, 719, L5
Langanke, K., & Martínez-Pinedo, G. 2001, At. Data Nucl. Data Tables, 79, 1
Lesaffre, P., Han, Z., Tout, C. A., Podsiadlowski, P., & Martin, R. G. 2006, MNRAS, 368, 187
Li, W., Bloom, J. S., Podsiadlowski, P., et al. 2011, Nature, 480, 348
Lisewski, A. M., Hillebrandt, W., & Woosley, S. E. 2000, ApJ, 538, 831
Livio, M. 2000, in Type Ia Supernovae, Theory and Cosmology, ed. J. C. Niemeyer & J. W. Truran (Cambridge: Cambridge Univ. Press), 33
Maeda, K., Röpke, F. K., Fink, M., et al. 2010, ApJ, 712, 624
Mannucci, F., Della Valle, M., & Panagia, N. 2006, MNRAS, 370, 773
Mazzali, P. A., & Podsiadlowski, P. 2006, MNRAS, 369, L19
Meakin, C. A., Seitenzahl, I., Townsley, D., et al. 2009, ApJ, 693, 1188
Minkowski, R. 1941, PASP, 53, 224
Neill, J. D., Sullivan, M., Howell, D. A., et al. 2009, ApJ, 707, 1449
Niemeyer, J. C. 1999, ApJ, 523, L57
Niemeyer, J. C., & Hillebrandt, W. 1995, ApJ, 452, 769
Niemeyer, J. C., & Woosley, S. E. 1997, ApJ, 475, 740
Nomoto, K., Saio, H., Kato, M., & Hachisu, I. 2007, ApJ, 663, 1269
Nomoto, K., Thielemann, F.-K., & Yokoi, K. 1984, ApJ, 286, 644
Nugent, P. E., Sullivan, M., Cenko, S. B., et al. 2011, Nature, 480, 344
Oda, T., Hino, M., Muto, K., Takahara, M., & Sato, K. 1994, At. Data Nucl. Data Tables, 56, 231
Perlmutter, S., Aldering, G., Goldhaber, G., et al. 1999, ApJ, 517, 565
Phillips, M. M. 1993, ApJ, 413, L105
Pinto, P. A., & Eastman, R. G. 2000, ApJ, 530, 744
Piro, A. L., & Bildsten, L. 2008, ApJ, 673, 1009
Piro, A. L., & Chang, P. 2008, ApJ, 678, 1158
Plewa, T., Calder, A. C., & Lamb, D. Q. 2004, ApJ, 612, L37
Poludnenko, A. Y., Gardiner, T. A., & Oran, E. S. 2011, Phys. Rev. Lett., 107, 054501
Poludnenko, A. Y., & Oran, E. S. 2011a, Combust. Flame, 157, 995
Poludnenko, A. Y., & Oran, E. S. 2011b, Combust. Flame, 158, 301
Pope, S. B. 1987, Annu. Rev. Fluid Mech., 19, 237
Riess, A. G., Filippenko, A. V., Challis, P., et al. 1998, AJ, 116, 1009
Riess, A. G., Macri, L., Casertano, S., et al. 2011, ApJ, 730, 119
Röpke, F. K. 2006, in Reviews in Modern Astronomy, Vol. 19, ed. S. Roeser (Weinheim: Wiley-VCH), 127
Röpke, F. K. 2007, ApJ, 668, 1103

Röpke, F. K., Gieseler, M., Reinecke, M., Travaglio, C., & Hillebrandt, W. 2006, A&A, 453, 203
Röpke, F. K., & Hillebrandt, W. 2005, A&A, 429, L29
Röpke, F. K., & Niemeyer, J. C. 2007, A&A, 464, 683
Röpke, F. K., Seitenzahl, I. R., Benitez, S., et al. 2011, Prog. Part. Nucl. Phys., 66, 309
Scalzo, R. A., Aldering, G., Antilogus, P., et al. 2010, ApJ, 713, 1073
Scannapieco, E., & Bildsten, L. 2005, ApJ, 629, L85
Schmidt, W., Ciaraldi-Schoolmann, F., Niemeyer, J. C., Röpke, F. K., & Hillebrandt, W. 2010, ApJ, 710, 1683
Schmidt, W., Niemeyer, J. C., & Hillebrandt, W. 2006a, A&A, 450, 265
Schmidt, W., Niemeyer, J. C., Hillebrandt, W., & Röpke, F. K. 2006b, A&A, 450, 283
Seitenzahl, I. R., Ciaraldi-Schoolmann, F., & Röpke, F. K. 2011, MNRAS, 414, 2709
Seitenzahl, I. R., Meakin, C. A., Townsley, D. M., Lamb, D. Q., & Truran, J. W. 2009a, ApJ, 696, 515
Seitenzahl, I. R., Townsley, D. M., Peng, F., & Truran, J. W. 2009b, At. Data Nucl. Data Tables, 95, 96
Straniero, O., Domínguez, I., Imbriani, G., & Piersanti, L. 2003, ApJ, 583, 878
Sullivan, M., Guy, J., Conley, A., et al. 2011, ApJ, 737, 102
Timmes, F. X., & Swesty, F. D. 2000, ApJS, 126, 501
Townsley, D. M., Calder, A. C., Asida, S. M., et al. 2007, ApJ, 668, 1118
Townsley, D. M., Jackson, A. P., Calder, A. C., et al. 2009, ApJ, 701, 1582
Truran, J. W., Arnett, W. D., & Cameron, A. G. W. 1967, Can. J. Phys., 45, 2315
Vladimirova, N., Weirs, G., & Ryzhik, L. 2006, Combust. Theory Modelling, 10, 727
Woosley, S. E. 1990, in Supernovae, ed. A. G. Petschek (New York: Springer-Verlag), 182
Woosley, S. E. 2007, ApJ, 668, 1109
Woosley, S. E., Kasen, D., Blinnikov, S., & Sorokina, E. 2007, ApJ, 662, 487
Woosley, S. E., Kerstein, A. R., Sankaran, V., Aspden, A. J., & Röpke, F. K. 2009, ApJ, 704, 255
Yuan, F., Quimby, R. M., Wheeler, J. C., et al. 2010, ApJ, 715, 1338